

MIT Open Access Articles

Screening for modulators of the cellular composition of gut epithelia via organoid models of intestinal stem cell differentiation

The MIT Faculty has made this article openly available. **Please share** how this access benefits you. Your story matters.

Citation: Mead, Benjamin E, Hattori, Kazuki, Levy, Lauren, Imada, Shinya, Goto, Norihiro et al. 2022. "Screening for modulators of the cellular composition of gut epithelia via organoid models of intestinal stem cell differentiation." Nature Biomedical Engineering, 6 (4).

As Published: 10.1038/S41551-022-00863-9

Publisher: Springer Science and Business Media LLC

Persistent URL: <https://hdl.handle.net/1721.1/147041>

Version: Final published version: final published article, as it appeared in a journal, conference proceedings, or other formally published context

Terms of use: Creative Commons Attribution 4.0 International license





OPEN

Screening for modulators of the cellular composition of gut epithelia via organoid models of intestinal stem cell differentiation

Benjamin E. Mead^{1,2,3,4,5,6,7,14}, Kazuki Hattori^{1,2,3,8,14}, Lauren Levy^{1,2,3}, Shinya Imada², Norihiro Goto², Marko Vukovic^{1,2,3,4,5,6,7,9}, Daphne Sze^{2,3,8}, Conner Kummerlowe^{1,2,3,4,5,7}, Juan D. Matute^{10,11}, Jinzhi Duan¹⁰, Robert Langer^{1,2,5,12}, Richard S. Blumberg¹⁰, Jose Ordovas-Montanes^{3,4,9}, Ömer H. Yilmaz^{1,2,13}, Jeffrey M. Karp^{1,3,4,8} ✉ and Alex K. Shalek^{1,2,3,4,5,6,7} ✉

The cellular composition of barrier epithelia is essential to organismal homeostasis. In particular, within the small intestine, adult stem cells establish tissue cellularity, and may provide a means to control the abundance and quality of specialized epithelial cells. Yet, methods for the identification of biological targets regulating epithelial composition and function, and of small molecules modulating them, are lacking. Here we show that druggable biological targets and small-molecule regulators of intestinal stem cell differentiation can be identified via multiplexed phenotypic screening using thousands of miniaturized organoid models of intestinal stem cell differentiation into Paneth cells, and validated via longitudinal single-cell RNA-sequencing. We found that inhibitors of the nuclear exporter Exportin 1 modulate the fate of intestinal stem cells, independently of known differentiation cues, significantly increasing the abundance of Paneth cells in the organoids and in wild-type mice. Physiological organoid models of the differentiation of intestinal stem cells could find broader utility for the screening of biological targets and small molecules that can modulate the composition and function of other barrier epithelia.

Barrier tissues interact with the external environment and protect from it. These vital functions are accomplished by specialized epithelial cells, descendant from epithelial stem cells, and are supported by stromal and immune cell populations. Balanced cellular composition in these barrier tissues is critical for host health. In the upper respiratory tract and skin, for example, changes in epithelial cellularity arising from aberrant stem cell differentiation can precipitate inflammatory diseases^{1,2}. Similarly, shifts in the composition and quality of mature epithelial cells are known to occur in the colon and small intestine of patients suffering from inflammatory bowel disease³. Cellular differentiation from the intestinal stem cell (ISC) niche is fluid and responsive to both physiologic and pathologic stimuli⁴, and ISCs have a capacity to integrate dietary and immune-derived signals to modulate their self-renewal and differentiation into specific secretory lineages⁵⁻⁷. Given this plasticity and the importance of barrier cellularity, barrier stem cells are a compelling target for therapeutic development.

To support discovery efforts to modulate epithelial barriers across the spectrum of health and disease, there is a need to scale approaches that can identify druggable biological targets that regulate epithelial composition and function. Ideally, these efforts would take place as close to the patient as possible. However, testing in vivo is poorly scaled and complicated by ethical boundaries.

High-throughput testing is possible in cell lines, but they are limited by poor representation of tissue-level biology, which can hinder translation⁸. To empower true target identification, we require in vitro cellular models that faithfully recapitulate the barrier tissue cells and functional processes that occur in vivo.

Modelling of epithelial barrier tissues, such as the intestine, in vitro has advanced substantially over the past decade thanks to the widespread development of organoid models. Intestinal organoids—broadly defined as three-dimensional (3D), stem cell-derived, tissue-like cellular structures—have proven to be valuable models of the adult stem cell niche, and preserve known developmental pathways in stem cell differentiation^{9,10}. The addition of well-characterized small molecules to culture media enables intestinal organoids to be further enriched for ISCs and can also be used to drive differentiation down specific lineages via physiologically meaningful cues, such as the modulation of Wnt and Notch signalling pathways¹⁰. Use of such rationally directed differentiation has been applied to induce functional Paneth cells (an antimicrobial-producing cell of the small intestinal crypt and proximal colon in humans) from enriched ISCs in vitro¹¹. Further, foundational work with murine intestinal organoids has illuminated the intricacies of how these multicellular systems initially self-assemble¹², providing an insightful landscape into the phenotypic states accessible to these models¹³.

¹Harvard-MIT Program in Health Sciences and Technology, MIT, Cambridge, MA, USA. ²Koch Institute for Integrative Cancer Research, MIT, Cambridge, MA, USA. ³Harvard Stem Cell Institute, Cambridge, MA, USA. ⁴Broad Institute of MIT and Harvard, Cambridge, MA, USA. ⁵Institute for Medical Engineering and Science, MIT, Cambridge, MA, USA. ⁶Department of Chemistry, MIT, Cambridge, MA, USA. ⁷Ragon Institute of MGH, MIT and Harvard, Cambridge, MA, USA. ⁸Engineering in Medicine, Department of Medicine, Brigham and Women's Hospital, Harvard Medical School, Boston, MA, USA. ⁹Division of Gastroenterology Boston Children's Hospital, Program in Immunology, Harvard Medical School, Boston, MA, USA. ¹⁰Division of Gastroenterology, Department of Medicine, Brigham and Women's Hospital, Harvard Medical School, Boston, MA, USA. ¹¹Division of Neonatology, Department of Pediatrics, MGH Harvard Medical School, Boston, MA, USA. ¹²Department of Chemical Engineering, MIT, Cambridge, MA, USA. ¹³Department of Pathology, MGH, Harvard Medical School, Boston, MA, USA. ¹⁴These authors contributed equally: Benjamin E. Mead, Kazuki Hattori. ✉e-mail: jmkarp@bwh.harvard.edu; shalek@mit.edu

Yet, organoid models are dynamic, cellularly and structurally heterogeneous, and typically require complex and costly experimental manipulations. This has limited their application as a screening tool to inform *in vivo* tissue biology. To date, organoids have primarily been used at scale to either decipher fundamentals of organoid biology^{13,14} or in the context of malignancy where the therapeutic phenotype (for example, growth inhibition) is easily measured^{15–17}. Thus, while such work has been foundational towards harnessing organoids for screening, it has not yet yielded a scalable start-to-finish discovery pipeline to identify tissue-modifying agents that operate from initial discovery to *in vivo* validation.

We sought to test whether a framework utilizing organoid models could be used to identify translatable barrier tissue-modifying small molecules. Broadly, such a framework can be described in 4 steps: (1) choosing a specific physiological process that is well-modelled by an organoid and perform a phenotypic screen for marker(s) of desired effect; (2) prioritizing lead compound(s) through a rigorous statistical approach and validating compound(s) in orthogonal assays; (3) exploring compound-mediated biology in organoid model with a high-content assay (for example, single-cell RNA-seq) to examine putative mechanism of action; and (4) where cellular mechanisms dictate potential for translation, testing select compound(s) *in vivo* to validate intended effect.

More specifically, we aimed to screen for pharmaceutically actionable biological targets that mediate a physiological differentiation process independent of major niche-associated pathways. We adapted organoids for phenotypic high-throughput screening through the reduction of model complexity around a well-structured hypothesis – here, to modulate physiological Paneth cell differentiation – that incorporates links to *in vivo* tissue biology^{18,19}. Searching for unreported targets that enhance Paneth cell differentiation and increase their abundance in the native tissue may be therapeutically valuable. Declines in Paneth cell quality and number are observed in inflammatory bowel disease^{20–22}, necrotizing enterocolitis²³, environmental enteric dysfunction²⁴ and intestinal manifestations of graft versus host disease (GvHD)²⁵. Additionally, treatment with R-spondin 1, a potentiator of Wnt signalling, can resolve dysbiosis seen in mice with GvHD by stimulating ISCs to differentiate into Paneth cells²⁶, but is challenging to apply clinically as Wnt activation is implicated in precancerous hyperplasia²⁷. Other signalling pathways known to drive Paneth cell differentiation, including Notch signalling, face similar challenges²⁸.

Through the development and application of a screening framework, we identify previously unreported targets and associated agents that may meaningfully enhance *in vivo* Paneth cell abundance. Following initial screening efforts, we perform robust cross-species *in vitro* investigation of our most potent hit to identify a key lead and its underlying biology. From there, we demonstrate translation in a murine model, showing a specific increase in Paneth cell abundance *in vivo*. Overall, our work defines an extendable paradigm with which to discover targets and their cognate pharmacophores for rationally modulating epithelial barrier cellularity.

Results

To screen for biological targets that may regulate Paneth cell differentiation *in vitro* and translate *in vivo*, we developed a scalable approach (thousands of samples) to scan a target-annotated small-molecule library and measure specific changes of a single cell type (Paneth cells) within a dynamic (differentiating) and heterogeneous (organoid) system, which represents the physiological differentiation environment (Fig. 1a). To model physiologically driven Paneth cell differentiation, we employed small-molecule-mediated enrichment and differentiation of murine adult-derived small intestinal organoids from ISCs (media formulated as ENR + CV – EGF, Noggin, R-spondin 1, CHIR99021, Valproic Acid – Methods) to Paneth cells (media formulated as ENR + CD – EGF, Noggin,

R-spondin 1, CHIR99021, DAPT – Methods), as we have previously shown^{10,11}. To scale this model, we adapted conventional 3D organoid culture into a 2.5D pseudo-monolayer, where ISC-enriched organoids are partially embedded on the surface of a thick layer of Matrigel at the Matrigel–media interface, rather than fully encapsulated in the Matrigel structure—an approach similar to others previously reported^{29,30}. This technique enables Matrigel plating, cell seeding and media additions to be performed in a high-throughput, fully-automated, 384-well plate format and allows for analyte secretion directly into cell culture media (Extended Data Fig. 1a). To measure changes in Paneth cell abundance or quality, we used a validated assay measuring lysozyme (LYZ, an antimicrobial secreted specifically by Paneth cells) activity in cell culture media via a commercially available fluorescent reporter reaction that is readily implemented via automated liquid handling (Methods)¹¹. Specifically, for each well, we first measured basally secreted LYZ (LYZ.NS), then carbachol (CCh)-induced secretion (LYZ.S) and finally, cellular adenosine triphosphate (ATP) as a measure of relative cell number per well. We assayed both stimulant-induced (LYZ.S – total cellular LYZ) and basal (LYZ.NS – constitutively secreted LYZ) secretion to distinguish compounds that may mediate changes in Paneth cell quality or secretion (LYZ.NS and LYZ.S uncorrelated) versus changes in Paneth cell abundance (LYZ.NS and LYZ.S correlated) (Extended Data Fig. 1b).

Using this pipeline, we performed a primary screen with a target-selective inhibitor library of 433 annotated compounds with high specificity to 184 unique biological targets (Supplementary Dataset 1) over a 6d differentiation starting from ISC-enriched organoid precursors ($n=3$ biological replicates originating from unique murine donors). In total, our proof-of-concept screen assayed 5,760 unique samples with the triplexed functional assay. Small molecules were added into distinct wells at 4 concentrations per compound (80 nm to 10 μ M range) at day 0 and day 3, and on day 6, we measured basal and induced secretion of LYZ in media supernatants, as a specific marker of Paneth cell enrichment, as well as ATP. To verify multiplexed assay performance in the screen, randomly distributed dimethyl sulfoxide (DMSO)-treated wells and no-cell wells were placed in each screening plate, and DMSO-treated wells were exposed to CCh (stimulated) in varying orders across the two LYZ assays (Fig. 1a).

Following normalization of all measured wells (Methods), each assay had an approximate-normal distribution, with lower-value tails corresponding to toxic compounds (Extended Data Fig. 1b). Treatments across biological replicates and assays were well correlated, with Pearson correlation values between screen plates ranging from 0.50 to 0.74 (Extended Data Fig. 1c). Randomly placed control (DMSO) wells (labeled A,B,C,D based on stimulation order) had significantly higher ATP readings than no-cell wells ($P<0.0001$), and in the LYZ.NS and subsequent LYZ.S assays, supernatant LYZ was significantly higher in 10 μ M CCh-stimulated control wells than in basal control wells (A+B vs C+D LYZ.NS $P<0.0001$, A vs B LYZ.S $P<0.05$), which in turn were significantly higher than no-cell wells (no-cell vs A+B LYZ.NS $P<0.0001$, no-cell vs A LYZ.S $P<0.0001$) (Extended Data Fig. 1d). Small but statistically significant differences in control well assays across the entire screen are probably due to intrinsic variability in phenotypic screening in an organoid system, where precise control over cell number is limited, which in turn may impact non-normalized LYZ secretion measures. Accordingly, we chose to employ a strictly standardized mean difference (SSMD) methodology comparing replicate treatments to whole-plate controls so we could explicitly base our hit decision criteria within each assay on power calculations.

We next sought to define which molecules meaningfully increased Paneth cell abundance. We defined primary screen ‘hits’ as having replicate SSMDs greater than the calculated optimal critical value ($\beta_{\alpha_1}=0.997$) in both LYZ.NS and LYZ.S assays (Fig. 1b

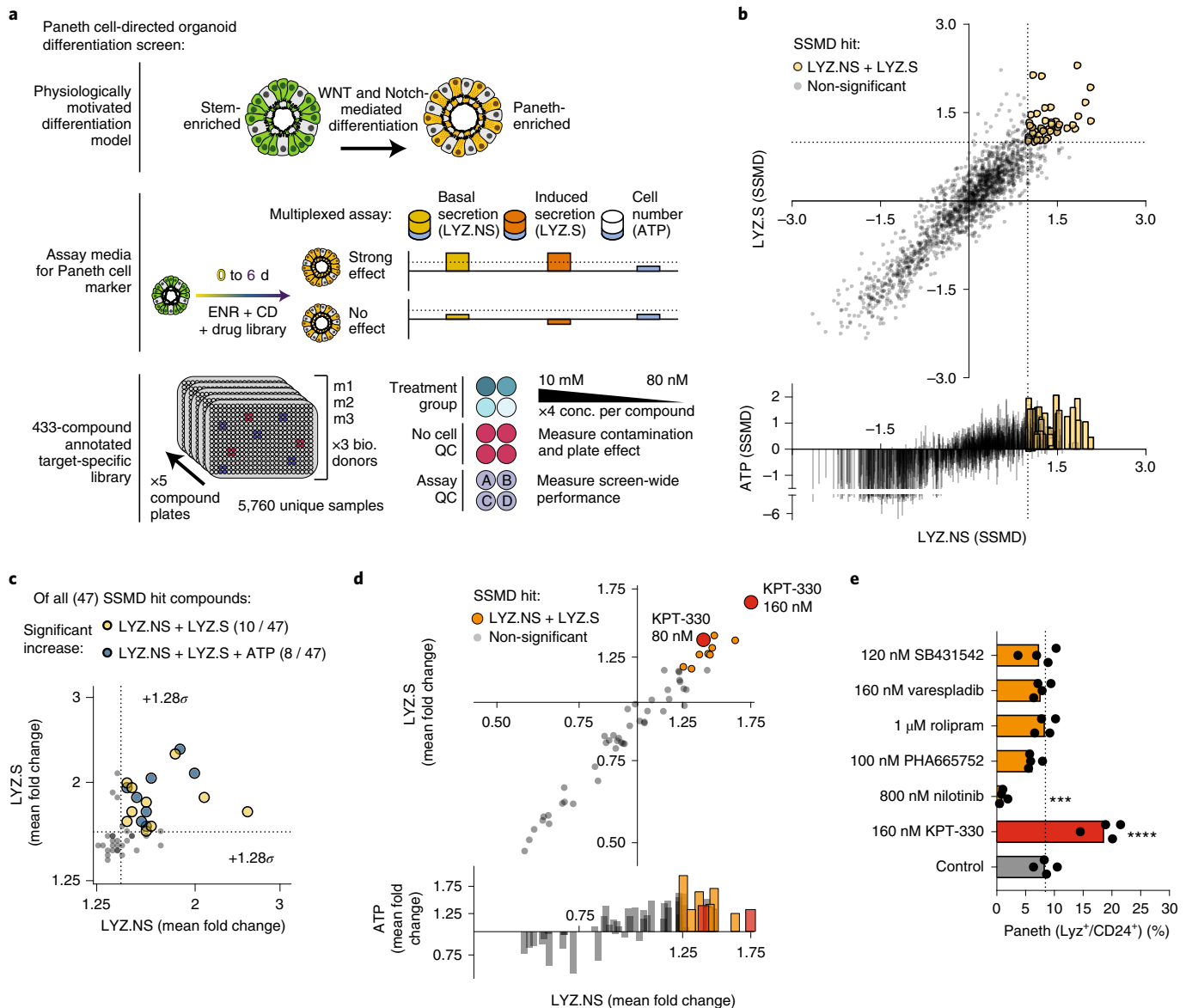


Fig. 1 | High-throughput organoid differentiation screen reveals pro-Paneth function compounds. **a**, Stem-enriched to Paneth-enriched (ENR+CD) organoid differentiation-modulating small-molecule screen (top row) assayed with multiplexed functional secretion, both basal (LYZ.NS) and 10 μ M carbachol-stimulated (induced) lysozyme (LYZ.S) secretion, and cell number (ATP) on day 6 (middle row). Screened compounds (433) dosed at 4 concentrations (80 nM to 10 mM) were randomly distributed across 5 plates with interspersed quality control (QC) wells including both no cell and stimulated and non-stimulated (A,B,C,D) (bottom row), with the full screen repeated with organoids derived from 3 murine donors (m1–m3). **b**, Replicate strictly standardized mean difference (SSMD) for each assay in the primary screen, each point representing the SSMD from 3 replicates of 3 biological donors relative to the whole-plate control. Coloured points are hits above the false positive limit- and false negative limit-determined cutoff (dotted lines) in both LYZ.NS and LYZ.S assays. **c**, Mean fold change of assay effect for hits in LYZ.S and LYZ.NS (yellow) or all three assays (blue) in the primary screen; only points above 1.28 s.d. (σ) (dotted lines) of all treatment mean fold changes for LYZ.S and LYZ.NS are deemed significantly increased. **d**, Mean fold change for each assay in the secondary validation screen ($N=8$ well replicates, relative to DMSO controls); orange, treatments advanced for profiling; red, most potent compound, KPT-330. **e**, Flow cytometry for the mature Paneth cell fraction of all live cells in 3D-cultured intestinal organoids treated with 6 hit compounds during 6 d of culture in ENR+CD media. Paneth cells were identified as lysozyme-positive and CD24-mid cells. Means and individual values are shown ($N=4$); dotted line represents the average Paneth cell fraction in control samples. One-way analysis of variance (ANOVA) post-hoc Dunnett's multiple comparisons test: **** $P < 0.0001$, *** $P = 0.001$.

and Methods). This was determined as the intersection minimizing false positive and false negative levels (FPL and FNL error = 0.084) for upregulation of SSMD-based decisions³¹. The 47 hits correspond to treatment–dose (grouped by biological replicate) combinations that had a significant increase in LYZ.NS and LYZ.S without regard to viability (note that most hits based on these criteria had positive effects on cellular ATP). Hits were refined further to

15 treatment–dose combinations with the greatest biological effect, determined by a fold change in the top 10% of values for both LYZ assays relative to the plate (z -score > 1.282). Thus, 15 drugs (covering 18 treatment–dose conditions) from 13 unique annotated targets were identified as primary screen hits (Fig. 1c). For annotated targets with more than one hit, the most potent treatment–dose was selected for further investigation.

To validate primary screen hits against an ENR+CD (not plate) control, while refining dose-response ranges and narrowing hits to only the most potent activators of increased LYZ secretion, we performed a secondary screen with the 13 primary screen hit compounds. Compounds were tested at a narrowed dose range around each treatment's identified optimal dose from the primary screen (4× below, 2× below and above). Hits in the validation screen were chosen as SSMDs greater than the calculated optimal critical value ($\beta_{ai} = 0.889$) in both LYZ.NS and LYZ.S assays, with 6 compounds passing this threshold (Extended Data Fig. 1e). The same treatment-dose conditions passing the SSMD threshold also had the greatest biological effect, and in particular one compound, KPT-330, a known Exportin 1 (XPO1) inhibitor (a nuclear exporter that regulates the efflux of nuclear export signal (NES)-tagged cargoes, including many transcription factors, from the nucleus³²), had two doses representing the greatest and near-greatest biological effect (~50–75% increases in LYZ.NS and LYZ.S relative to ENR+CD control) (Fig. 1d).

The results of primary and validation screening reflect a mixture of potential effects that may cause increases in total LYZ secretion. This includes contributions from: enhanced Paneth cell differentiation, altered Paneth cell quality and changes in total cell number concurrent with differentiation. To better inform how the 6 hit compounds increased total secreted LYZ, and to isolate only those that enhance Paneth differentiation robustly, we utilized flow cytometry to measure changes in Paneth cell representation within treated organoids. Concurrently, to ensure that we do not select compounds that manifest their behaviour only in specific in vitro settings, we performed the analyses in the conventional 3D culture method, controlling for 2.5D culture system-specific effects. Live Paneth cells were identified as LYZ-high, CD24-mid, side scatter-high (SSC-high) (Extended Data Fig. 1f). Only KPT-330—the most potent compound in validation screening—significantly enhanced the mature Paneth cell population within differentiating organoids, suggesting that KPT-330 induces Paneth differentiation (Fig. 1e). Of the 5 remaining compounds, Nilotinib excluded, none changed organoid composition and are probably driving changes in Paneth quality or are mediating effects dependent on 2.5D culture. Conversely, Nilotinib significantly decreased Paneth abundance while significantly increasing total cell number, suggesting that the overall increase in bulk LYZ secretion is an effect of increased proliferation, or 2.5D-mediated effect.

To examine whether our hits are dependent or independent of canonical stem cell niche signalling, we measured Paneth cell abundance in the ENR culture condition (removing CHIR99021 and DAPT, which mimic physiological Paneth differentiation through Wnt activation and Notch inhibition) in 3D (note that because

Paneth cells exist in an immature state within ENR, we were unable to robustly quantify Paneth cell number via flow cytometry, and instead used the LYZ secretion assay). The result mirrored our flow cytometry findings in the ENR+CD condition, suggesting that the identified compounds act independently of strong Wnt and Notch drivers, and that only KPT-330 is enhancing Paneth cell-specific activity in the conventional organoid culture condition (Extended Data Fig. 2a). Collectively, these results led us to focus solely on understanding the activity mechanism of KPT-330.

Support for XPO1 as a molecular target for enhancing Paneth cell differentiation. We next sought to support the predicted on-target activity of KPT-330 and investigate the dose-dependency of treatment in enhancing Paneth cell differentiation. Administration of KPT-330 below 160 nM for 6 d (note that higher concentrations proved toxic in primary screening) showed LYZ secretion increasing in a dose-dependent manner, with 160 nM of KPT-330 being the most effective dose among tested concentrations (Fig. 2a). Immunofluorescent (IF) imaging for LYZ+ Paneth cells within organoid cultures in ENR+CD+KPT-330 demonstrated an increase in Paneth cell number, in agreement with our results by both flow cytometry and LYZ secretion assay (Fig. 2b,c). Furthermore, this pro-Paneth differentiation effect was also observed by IF imaging in the ENR media +/- KPT-330 (Extended Data Fig. 2b,c). To demonstrate that XPO1 is the primary biological target of KPT-330, we used two additional XPO1 inhibitors: KPT-8602 and Leptomycin B³³. Flow cytometry and IF imaging results show both KPT-8602 and Leptomycin B increasing the proportion of Paneth cells in the organoids (Fig. 2d–g). LYZ secretion assays with the additional XPO1 inhibitors show similar Paneth cell enrichments in both conventional (ENR) and Paneth-differentiating (ENR+CD) culture conditions (Fig. 2h and Extended Data Fig. 2d). Western blotting for intercellular LYZ per unit weight also confirms enrichment with each of the known XPO1 inhibitors in both conventional (ENR) and Paneth-differentiating (ENR+CD) culture conditions (Fig. 2i and Extended Data Fig. 2e), consistent with LYZ secretion, IF imaging and flow cytometry analyses.

KPT-330 (and KPT-8602) is a selective inhibitor of nuclear export (SINE); these molecules act by suppressing the XPO1-regulated nuclear export of multiple proteins and mRNAs from the nucleus to the cytoplasm—including genes involved in stem cell maintenance and differentiation as well as inflammatory stress response³⁴. Additionally, XPO1 is known to regulate the cell cycle through its export-independent role in the regulation of mitosis³⁵. On the basis of this evidence, we hypothesized that XPO1 inhibition via KPT-330 might provide for enhanced Paneth cell differentiation by directing ISCs to modulate their differentiation trajectories through

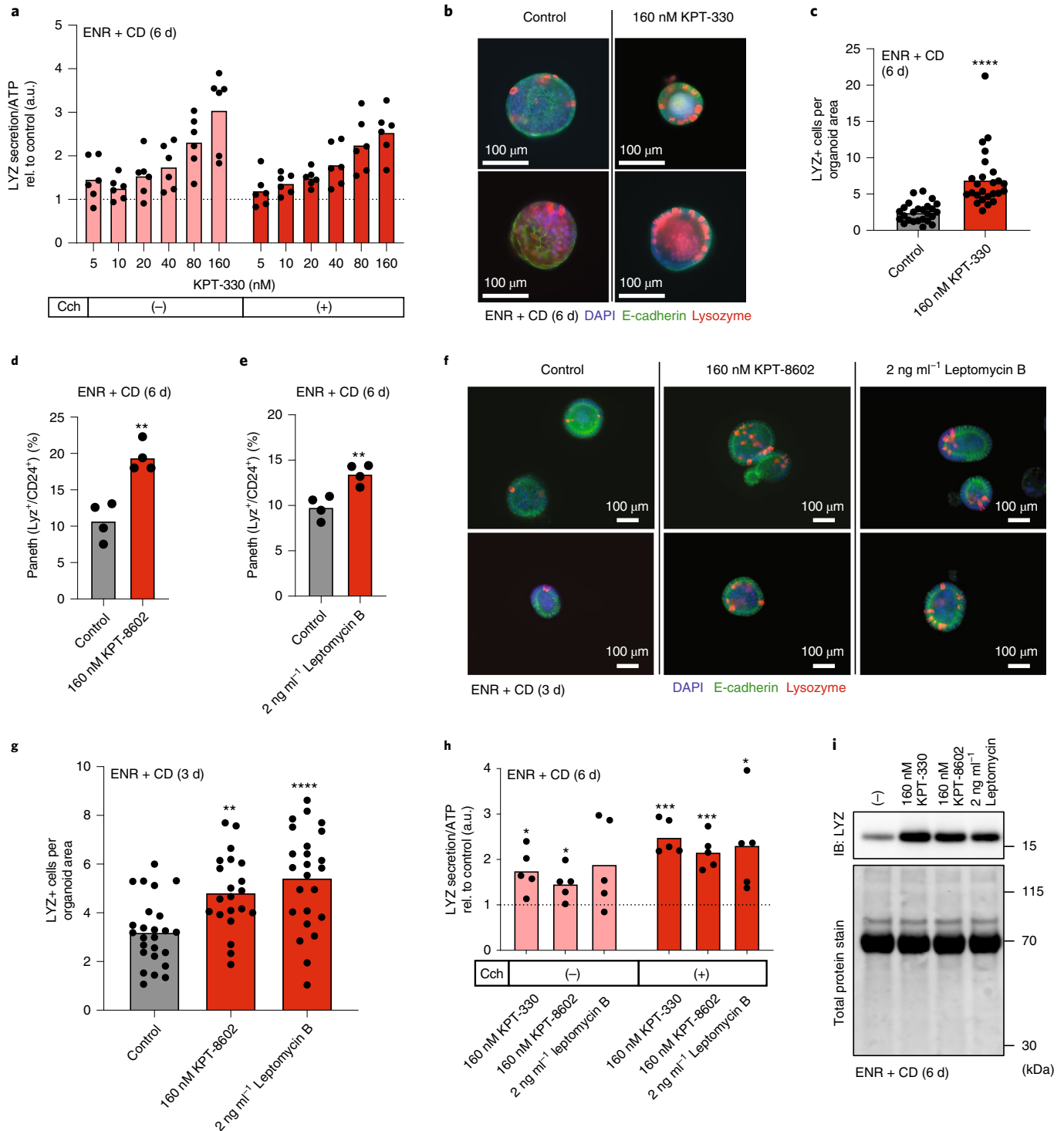
Fig. 2 | Small-molecule inhibition of XPO1 enhances Paneth cell differentiation. **a**, LYZ secretion assay for organoids differentiated in ENR+CD with increasing concentrations of KPT-330 for 6 d. Organoids were incubated in fresh basal media with or without 10 μ M Cch for 3 h on day 6. All data are normalized to ATP abundance and standardized to the control in each experiment. Means and individual values are shown ($N=6$), dotted line represents the control value (1). **b**, Representative immunofluorescence images of 25 total organoids differentiated in ENR+CD media with 160 nM KPT-330 for 6 d, Paneth cells are lysozyme (LYZ) positive. **c**, Quantification of immunofluorescence images for LYZ+ cells per organoid area for organoids differentiated in ENR+CD with 160 nM KPT-330 for 6 d. Means and individual values are shown ($N=25$ organoids). Unpaired two-tailed t -test: **** $P < 0.0001$. **d, e**, Flow cytometry for Paneth cell fraction (lysozyme-positive and CD24-mid cells) of all live cells in 3D-cultured intestinal organoids treated with 160 nM KPT-8602 (**d**) and 2 ng ml⁻¹ Leptomycin B (**e**) over 6 d culture in ENR+CD media. Means and individual values are shown ($N=4$). Unpaired two-tailed t -test: (**d**) ** $P = 0.0019$, (**e**) ** $P = 0.0051$. **f**, Representative immunofluorescence images of 25 total organoids differentiated in ENR+CD media with 160 nM KPT-8602 or 2 ng ml⁻¹ Leptomycin B for 3 d, Paneth cells are LYZ positive. **g**, Quantification of immunofluorescence images for LYZ+ cells per organoid area for organoids differentiated in ENR+CD with 160 nM KPT-8602 or 2 ng ml⁻¹ Leptomycin B for 3 d. Means and individual values are shown ($N=25$ organoids). One-way ANOVA post-hoc Dunnett's multiple comparisons test: **** $P = 0.0001$, ** $P = 0.0035$. **h**, LYZ secretion assay for organoids differentiated in ENR+CD with 160 nM KPT-330, 160 nM KPT-8602 or 2 ng ml⁻¹ Leptomycin B for 6 d. Organoids were incubated in fresh basal media with or without 10 μ M Cch for 3 h on day 6. All data were normalized to ATP abundance and standardized to the control in each experiment. Means and individual values are shown ($N=5$), dotted line represents the control value (1). One-sample t -test compared to 1, ordered left to right: * $P = 0.0242$, * $P = 0.0431$, *** $P = 0.0009$, *** $P = 0.0023$. **i**, Western blotting of intracellular LYZ (immunoblot - IB) in 3D-cultured intestinal organoids cultured in ENR+CD media in the presence of KPT-330, KPT-8602 or Leptomycin B for 6 d ($N=1$).

alterations in either developmental signalling within the nucleus and/or interfering with the cell cycle.

Single-cell RNA-sequencing of KPT-330-mediated differentiation reveals population shifts. To test the hypothesis that KPT-330 drives Paneth differentiation by altering ISC behaviour, we utilized single-cell RNA-sequencing (scRNA-seq) via Seq-Well S³ (ref. ³⁶). We performed a longitudinal comparison between untreated and KPT-330-treated organoids over a 6 d differentiation, with particular emphasis on early timepoints (Fig. 3a). We collected 17 samples at the following timepoints: 6 h (0.25 d) and 1, 2, 3, 4 or 6 d.

Each sample consists of single cells from >1,000 organoids from pre-differentiation ENR + CV organoids and both ENR + CD and ENR + CD + KPT-330 (160 nM) conditions. For timepoints beyond 2 d, media were refreshed every other day. The resulting dataset consists of 19,877 cells. Unique molecular identifier (UMI), percent mitochondrial and detected gene distributions are similar across samples, within acceptable quality bounds (genes >500, UMI <30,000, percent mitochondrial <35) (Extended Data Fig. 3a).

Following normalization, variable feature selection and principal component dimensional reduction (Methods), uniform manifold approximation and projection (UMAP) visualization of the complete



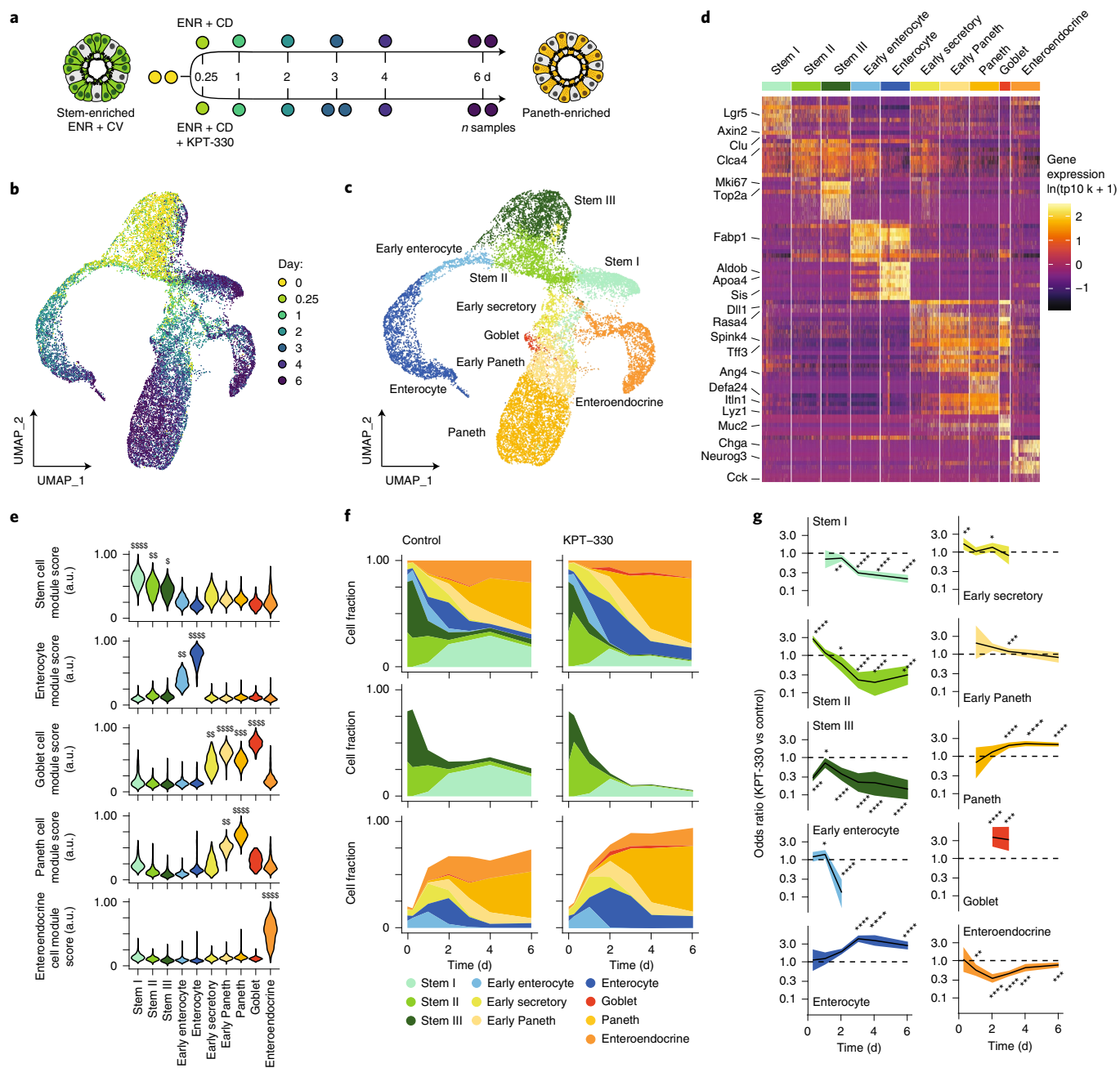


Fig. 3 | Longitudinal scRNA-seq profiling of organoid differentiation with KPT-330-mediated XPO1 inhibition. **a**, Stem-enriched (ENR+CV) to Paneth-enriched (ENR+CD) organoid differentiation in the presence and absence of 160 nM KPT-330; each circle represents a sample of organoids collected for scRNA-seq over the 6 d time course. **b, c**, UMAP of all samples labelled by differentiation timepoint (**b**) and annotated cell type (**c**). **d**, Log-normalized gene expression heat map for top 10 marker genes by cell type (by log fold change vs all others). **e**, Violin plots for all cell types representing module scores derived from gene sets enriched in *in vivo* intestinal stem cells, enterocytes, goblet cells, Paneth cells and enteroendocrine cells, with each score scaled on a range from 0 to 1. Effect size measured as Cohen’s *d*: \$0.5 < d < 0.8\$, \$\$0.8 < d < 1.2\$, \$\$\$1.2 < d < 2\$, \$\$\$\$d > 2\$. **f**, Organoid composition over time between untreated control and 160 nM KPT-330 treatment, for all cell types (top), stem cells (middle) and differentiating cells (bottom). **g**, Odds ratio enrichment and depletion over differentiation course based on Fisher exact testing, with 95% confidence interval plotted for each cell type relative to all others, dashed line at 1. FDR-adjusted Fisher exact testing: **P* < 0.05, ***P* < 0.01, ****P* < 0.001, *****P* < 0.0001, individual *P* values reported in source data.

dataset reveals the time-course structure, along with branches suggestive of distinct lineages arising over the course of differentiation (Fig. 3b). Tiered Louvain clustering separated the data into 10 clusters, which we manually annotated (Fig. 3c) on the basis of marker gene expression corresponding to canonical markers of intestinal epithelial cell types (Fig. 3d and Supplementary Dataset 2). Each cluster possessed similar quality metrics, suggesting that clusters

are driven by biological and not technical differences (Extended Data Fig. 3b). To contextualize and provide a more robust measure of cellular identity of our 10 clusters, we used lineage-defining gene sets from a murine small intestinal scRNA-seq atlas³⁷ to score for enrichment in gene-set expression (Extended Data Fig. 3c). The 10 clusters include 3 stem-like, 2 enterocyte, 1 early secretory, 1 goblet, 2 Paneth and 1 enteroendocrine, aligning with our expectation

that ENR + CD differentiation should enrich for secretory epithelial cells—principally Paneth and to a lesser extent goblet and enteroendocrine (Fig. 3e). To distinguish the 3 stem-like clusters and assess physiological relevance, we performed module scoring over gene sets identified to correspond to known ISC subsets *in vivo*⁶ (Extended Data Fig. 3e). We see alignment with the type III and type I ISCs, along with slight enrichment for a distinct type II (Extended Data Fig. 3e), although this population may also be an intermediate between stem I and III populations, sharing markers with both (Fig. 3d). Accordingly, we adopted this naming scheme to describe the 3 ISC populations: type I, enriched for canonical markers of ISCs (including LGR5); type III, distinguished by the high expression of cell cycle genes; and type II, appearing as a transitory or intermediate population between I and III.

We next explored changes in cell type representation between organoids treated with KPT-330 versus the control. In the combined dataset, we do not observe cell clusters unique to the KPT-330 treatment, but rather shifts in cluster composition (Extended Data Fig. 3f). Both conditions begin with over 75% of cells being either stem II or stem III. By day 2, stem I emerges, accounting for approximately 25% of the cells in the control condition, but a smaller proportion in KPT-330-treated organoids. Early enterocytes emerge at day 1, with the continued differentiation to enterocytes peaking at day 2 and becoming less prevalent by day 4. Early secretory, goblet and early Paneth populations appear to crest with enterocytes, followed by a transition to Paneth cells continuing to day 6 (Fig. 3f). To better quantify the differences in representation between the KPT-330 and control conditions over time, we performed Fisher's exact testing for each cell type relative to all others. This was done for each time-point when that cell type accounted for at least 0.5% of cells in both KPT-330 and control samples. We present the relative enrichment or depletion of a cell population with KPT-330 treatment over time as the odds ratio with a corresponding 95% confidence interval. KPT-330 treatment leads to a depletion of stem I, II, III and enteroendocrine cells over time, along with the corresponding enrichment of enterocytes, goblet (NB in this system goblet cells represent a very small fraction of total cells) and Paneth cells (Fig. 3g). The observed twofold enrichment in Paneth cells at day 6 mirrors our flow cytometry observations of a twofold increase in mature Paneth cells, while also showing the unexpected early enrichment of enterocytes and longer-term depletion of a subset of stem cells—the quiescent stem I population.

KPT-330 alters signalling and transcription factor activity across organoid cell types. To clarify the mechanism, determine potential mediators of putative KPT-330-mediated XPO1 inhibition in our system and better understand the differentiation process, we performed signalling pathway and upstream transcription factor (TF) inference on our scRNA-seq dataset using the PROGENy (to infer signalling pathway activity) and DoRothEA (to infer upstream TF activity) toolsets³⁸ (Methods). First, we examined how signalling pathway activity is distributed across the untreated cells of our differentiation system (Extended Data Fig. 4a), revealing expected pathways such as Wnt enriched across stem populations, and nuclear factor kappa-light-chain-enhancer of activated B cells (NFkB) and tumor necrosis factor alpha (TNF-alpha) enriched in enterocytes, suggesting that PROGENy captures meaningful biology. Within stem III, we observe high levels of mitogen-activated protein kinase (MAPK) and epidermal growth factor receptor (EGFR) signalling and low levels of stress-associated Trail and Hypoxia signalling. We next sought to understand how KPT-330 treatment effects signalling by computing the effect size (Cohen's *d*) of KPT-330 treatment for each pathway and cell type (Fig. 4a). We observe a pan-epithelial increase in stress-associated Trail signalling, stem III-specific increase in stress-associated hypoxia signalling, and secretory cell-specific increase in phosphatidylinositol 3-kinase (PI3K) signalling.

In addition, Janus kinase - signal transducer and activator of transcription protein (JAK-STAT) and transforming growth factor-beta (TGF-beta) are decreased across epithelial cell types, while EGFR and MAPK are decreased within the stem and early differentiating populations. These observations suggest decreases in mitogen signalling restricted to stem and progenitor populations, along with broader increases in cell stress responses. To determine potential transcriptional regulators associated with these changes, we performed UMAP visualization and Louvain clustering over inferred TF activity of the full single cell dataset, resulting in 7 clusters corresponding to upstream TF states (Fig. 4b). This upstream TF landscape captures heterogeneity associated with differentiation time and cell type (Extended Data Fig. 4b,c). The 7 states are distinguished by enrichment for cell cycle-associated TFs (0), known TFs of cell type-specific differentiation (2, enterocytes, Hnf4; and 5, enteroendocrine, Pdx1), TFs representing distinct stress responses (1, Atf4/6; and 6, Atf3, Thap11) and intermediary states of the aforementioned (3 and 4) (Supplementary Dataset 3 and Fig. 4c). Multiple clusters are enriched for distinct cell types associated with their cellular programmes (0, cycling stem; 2, enterocytes; 5, enteroendocrine), while others suggest programmes differentially induced by KPT-330 treatment (Paneth-enriched 1 and 4, and progenitor-enriched 6) (Fig. 4d,e). To quantify the differences in representation between KPT-330 and control conditions in each of the 7 transcriptional states, we performed Fisher's exact testing for each cell type relative to all others. This was done for each cluster where that cell type accounted for at least 10 cells in both KPT-330 and control samples. KPT-330 treatment leads to a depletion of cell cycle cluster 0 and enrichment in stress response cluster 6 across stems I, II, III, early enterocyte, early secretory and enteroendocrine cells, along with shifts in Paneth cells from clusters 1 to 4 (Fig. 4f). These analyses point to stem and progenitor-specific changes in the cell cycle and broader induction of stress responses following KPT-330-mediated XPO1 inhibition over the course of differentiation.

KPT-330 induces ISC differentiation via stress response and suppressed mitogen signalling. Compositional, signalling and upstream TF changes during differentiation with KPT-330 are consistent with XPO1 inhibition acting on stem II/III populations. In untreated organoids, the expression of *Xpo1* is significantly enriched in the cycling stem III population (Fig. 5a and Extended Data Fig. 5a), and the expression of genes known to contain a NES (which is required for the nuclear efflux via XPO1) is enriched in the stem cell populations—most significantly in stem III (Fig. 5b and Extended Data Fig. 5b)³⁹. XPO1 is known to mediate nuclear signalling processes including the MAPK pathway, nuclear factor of activated T-cells (NFAT), activator protein-1 (AP-1) and Aurora kinase activity during cell division^{32,34}. With this in mind, we observe the expression of many key mediators in these pathways within the stem populations (in agreement with our observations in Extended Data Fig. 4a), and see particular stem II and III expression in members of MAPK (*Mapk1*, *Mapk9*, *Mapk13*, *Mapk14*), NFAT (*Nfatc3*), AP-1 (*Fos*, *Jun*, *Atf1-6*) and Aurora kinases (*Aurka*, *Aurkb*) (Extended Data Fig. 5c).

To further validate whether the stem II/III population is the principal cellular target of KPT-330-mediated XPO1 inhibition, we leveraged the dynamic nature of our system and exposed organoids to KPT-330 over every 2, 4 and 6 d interval in the 6 d differentiation, and measured final abundance and function of mature Paneth cells at day 6, thereby inferring the relative effect of XPO1 inhibition on each cell type (Fig. 5c). Of all the 2 d KPT-330 treatments, day 0–2 results in the greatest enrichment in mature Paneth cells, with longer exposure after day 2 providing additional, albeit lesser enrichment. Furthermore, day 2–4 treatment produces moderate enrichment, while day 4–6 treatment is not different (by flow cytometry) or is slightly enriched (by LYZ secretion assay) from the

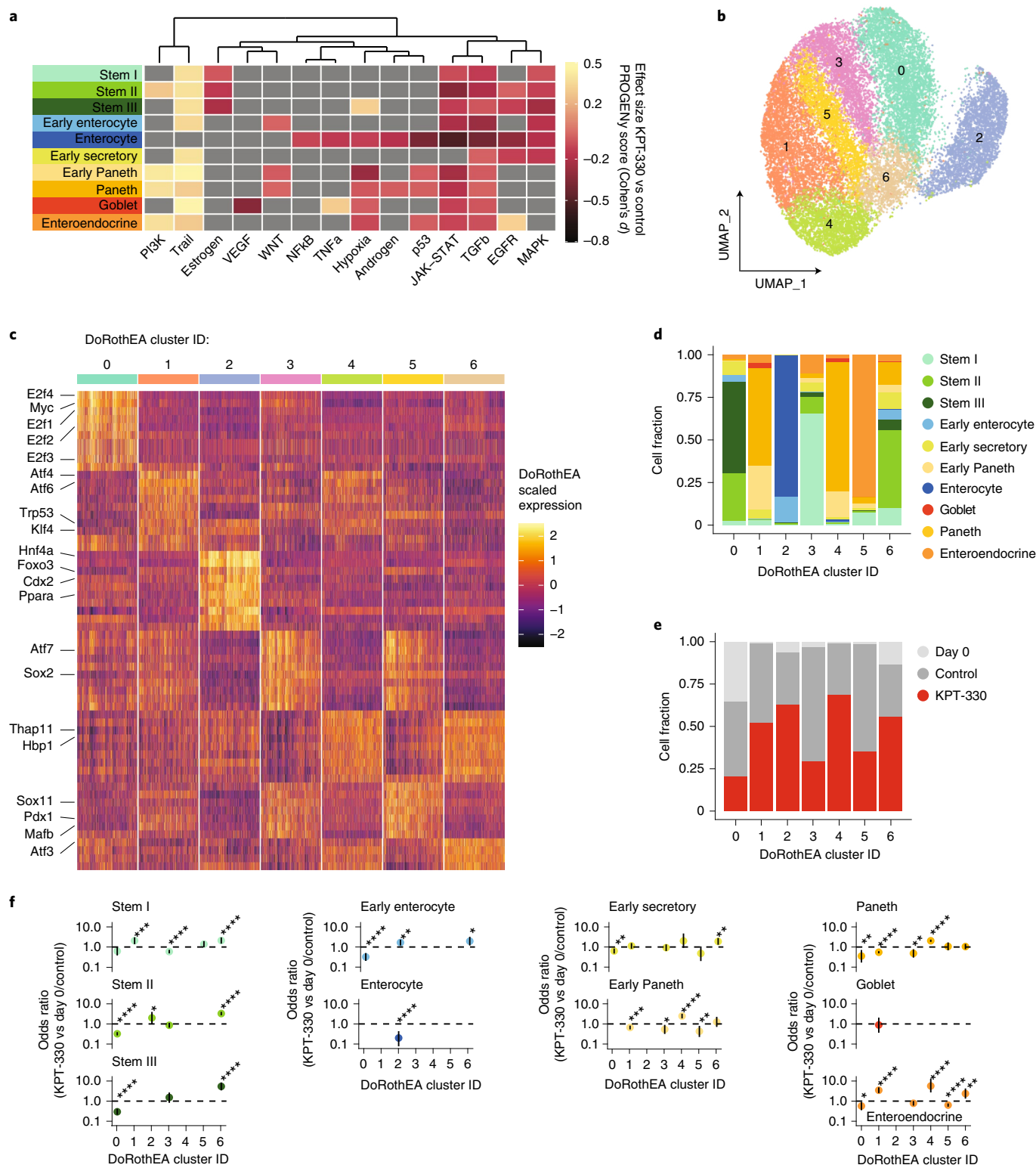


Fig. 4 | Inferred signalling pathway activity and upstream transcription factors associated with KPT-330-mediated differentiation. a, Heat map of Cohen's *d* effect sizes (greyed values $\leq \pm 0.2$) comparing differential PROGENy pathway activities between KPT-330 and non-treated cells within each cell type. **b**, Organoid scRNA-seq UMAP based on upstream TF prediction (DoRothEA) of all samples labelled by TF clustering (clusters named 0-6). **c**, Scaled predicted upstream transcription factor activity heat map for top 10 markers by TF cluster (by log fold change vs all others). **d, e**, Stacked bar chart for DoRothEA cluster by cell type (**d**) and KPT-treatment (**e**). **f**, Odds ratio enrichment and depletion by cell type and over DoRothEA cluster based on Fisher exact testing, with 95% confidence interval plotted for each cell type relative to all others, dashed line at 1. FDR-adjusted Fisher exact testing: * $P < 0.05$, ** $P < 0.01$, *** $P < 0.001$, **** $P < 0.0001$, individual *P* values reported in source data.

untreated (Fig. 5d and Extended Data Fig. 5d). Using an additional SINE, KPT-8602, we observe similar enrichment behaviour as KPT-330 (Extended Data Fig. 5e). These data are consistent with XPO1 inhibition altering stem II/III differentiation – the largest effects of XPO1 inhibition are concurrent with periods in the differentiation course where stem II/III populations are most abundant. However, these data also suggest that XPO1 inhibition may not be entirely stem-dependent, given the lesser but significant increases in Paneth cell number and function with later treatment, where stem II/III populations are greatly diminished.

To better understand the pleiotropic effects of KPT-330-mediated XPO1 inhibition that may mediate differentiation, we examined the differentially expressed genes between KPT-330-treated and untreated stem II/III populations in the earliest stages of differentiation when they are most abundant (day 0.25–2). Both the most significantly enriched (*Xpo1*) and depleted (*Kpnb1*, a nuclear importin) genes suggest that these cells are significantly impacted by KPT-330 treatment and are enacting changes in expression to re-establish homeostasis of nuclear cargo transit (Fig. 5e and Supplementary Dataset 4). Additional notable genes with significantly increased expression include *Arrdc3* (regulates proliferative processes), *Slc16a6* (principal transporter of ketone bodies; instructional in ISC fate decisions), *Tbgr1* (growth inhibitor) and *Atf3* (regulates stress response in ISCs)^{40–43}. Genes downregulated by KPT-330 treatment appear related to proliferation and the cell cycle, including the marker *Mki67*. In addition to substantial changes within early stem II/III populations, genes regulated by XPO1 inhibition—including *Xpo1*, *Atf3*, *Trp53* (p53), *Ccnd1*, *Cdk4/6* and *Cdkn1a* (p21)—have increased expression across all cell types (at all times), but with significant differences in the fraction of cells that express each gene (Extended Data Fig. 5f). This suggests that there are both stem II/III-specific responses and pan-epithelial responses to XPO1 inhibition.

To better contextualize the transcriptional response to KPT-330 treatment in stem II/III cells, we performed gene-set enrichment analyses (GSEA) using the v7 molecular signatures database (MSigDB) hallmark collection, which represent specific well-defined biological states or processes across systems^{44,45}. Significant gene sets with FDR < 0.05 reveal two major programmes differentially

enriched following KPT-330 treatment, with enrichment or depletion quantified through the GSEA normalized enrichment score (Fig. 5f and Supplementary Dataset 4). KPT-330 treatment suppresses programmes downstream of mitogen-driven signalling— notably, targets of E2F and MYC, as well as genes involved in the cell cycle (G2M checkpoint)—while upregulating programmes broadly resembling a stress response (NFκB signalling, hypoxia, inflammatory response), in agreement with our PROGENy and DoRothEA observations and with the known effects of XPO1 inhibition in the context of malignancy.

We next examined whether the responses embodied by the significant differentially expressed genes in stem II/III (day 0.25–2) may be pan-epithelial or restricted to the cycling stem II/III populations. The stress response module (differentially increased in stem II/III) is substantially increased across all cells during differentiation, with the greatest effect in the stem II/III as well as in early mature cell populations, and the lowest effect in the mature Paneth cells (Fig. 5g). Conversely, the mitogen signalling module (differentially decreased in stem II/III) is selectively decreased in stem II/III and early enterocyte populations relative to all others. This selectivity corresponds with our observation that the majority of mitogen signalling occurs within the proliferative stem II/III populations relative to the mature populations. As further evidence of altered mitogen signalling impacting stem II/III cells following XPO1 inhibition, we observe a decrease in a previously identified gene module⁴⁶ of active ISCs, and a corresponding increase of the quiescent ISC module in our early (day 0.25–2) stem II/III cells (Fig. 5h). Combined with our observation that XPO1 inhibition blocks the emergence of the quiescent stem I population, our data suggest a model wherein SINE-induced stress response and disruption of mitogen signalling instruct proliferative progenitors to exit the cell cycle and differentiate preferentially towards the Paneth lineage, while limiting the accumulation of quiescent stem I cells and enteroendocrine cells.

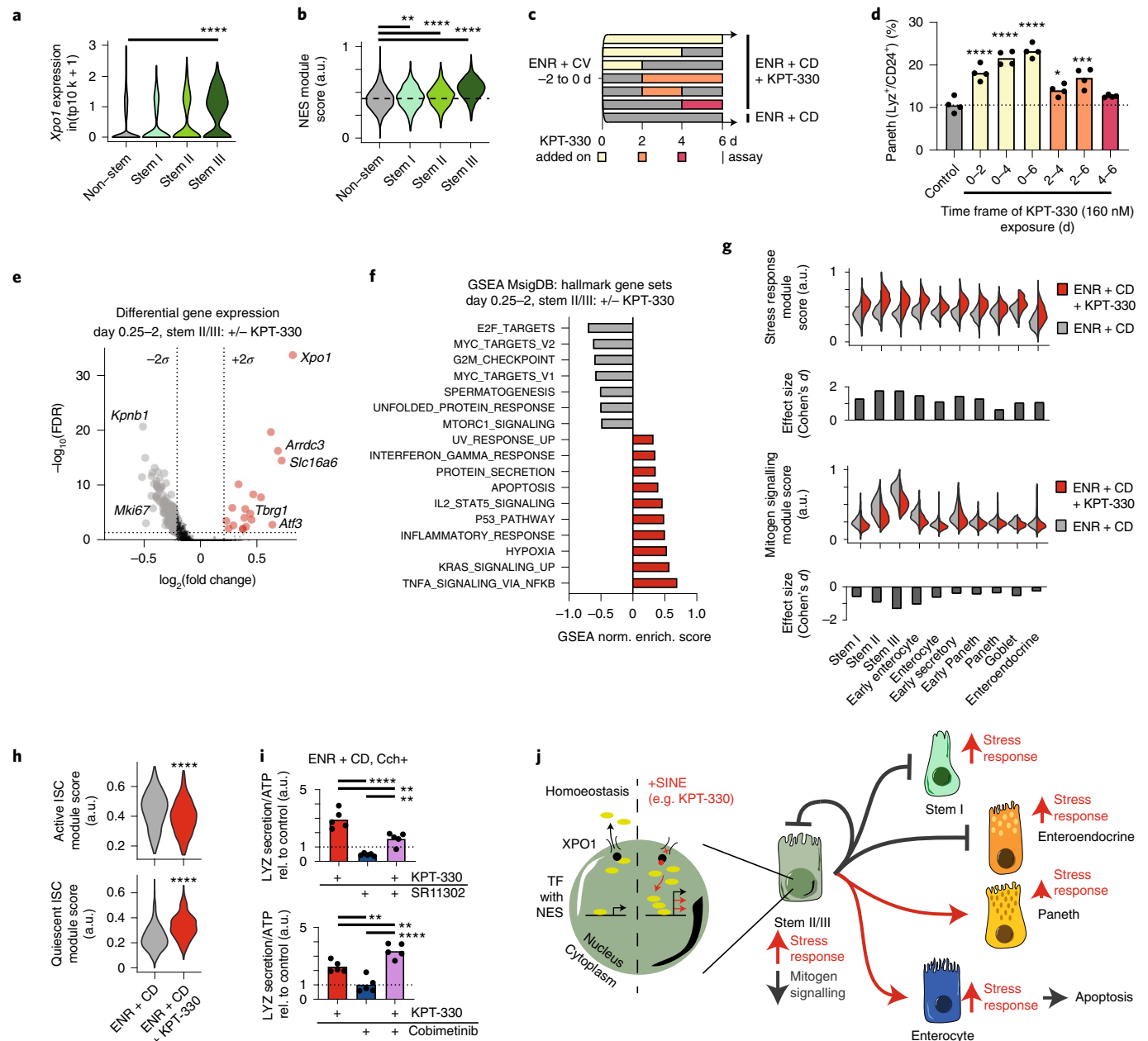
We sought to clarify this conceptual model with the use of additional small-molecule inhibitors known to modulate discrete components of our hypothesized differentiation process, namely: signalling through XPO1-associated stress response including AP-1 and p53, signalling within the MAPK pathway and finally,

Fig. 5 | KPT-330-mediated XPO1 inhibition drives stem cell-specific and pan-epithelial responses to induce differentiation. **a**, Violin plots of scRNA-seq log-normalized (transcripts per 10,000 – tp10k) expression of *Xpo1* in all untreated control cells split by non-stem and stem I/II/III annotations. Wilcoxon rank sum test, Bonferroni correction stem I/II/III vs non-stem: **** $P < 0.0001$. **b**, Violin plots of module scores over all cells derived from genes with known NES in all untreated control cells split by non-stem and stem I/II/III annotations, with each score scaled on a range from 0 to 1. One-way ANOVA post-hoc Dunnett's multiple comparisons test, ordered left to right: ** $P < 0.0063$, **** $P < 0.0001$. **c**, Time course of KPT-330 treatment of ENR+CD differentiating organoids, with treatments over every continuous 2, 4 and 6 d interval. **d**, Flow cytometry analyses of 3D-cultured intestinal organoids treated with KPT-330 for the indicated time frame during 6 d culture in ENR+CD media. Paneth cells were identified as lysozyme-positive and CD24-positive cells. Means and individual values are shown ($N = 4$), and the dotted line represents the average of the Paneth cell fractions in control samples. One-way ANOVA post-hoc Dunnett's multiple comparisons test, ordered left to right: **** $P < 0.0001$, * $P = 0.0323$, *** $P = 0.001$. **e**, Volcano plot of differentially expressed scRNA-seq log-normalized genes between KPT-330-treated and control cells within stem II/III populations in early timepoints (day 0.25–2). Red points, enriched in KPT-330 treatment; grey, enriched in control. Differential expression based on Wilcoxon rank sum test with significant \log_2 fold changes based on $\pm 2\sigma$ (dotted lines) of all genes; FDR (Bonferroni correction) cutoff $P < 0.05$. **f**, GSEA normalized enrichment score over all differentially expressed genes between KPT-330-treated and control cells within stem II/III populations in early timepoints (day 0.25–2). Gene sets shown from MSigDB Hallmark v7 with FDR < 0.05; red, enriched in KPT-330 treatment; grey, enriched in control. **g**, Violin plots split by KPT-330-treated and control for module scores derived from significantly enriched (stress response) and depleted (mitogen signalling) genes in KPT-330-treated and control cells within stem II/III populations in early timepoints (day 0.25–2); each score was scaled on a range from 0 to 1. Effect size (Cohen's d) for each module between KPT-330-treated and control modules within each cell type is represented in bar chart below violin plots. **h**, Violin plots of module scores derived from genes expressed in active and quiescent ISCs between KPT-330-treated and control cells within stem II/III populations in early timepoints (day 0.25–2); each score was scaled on a range from 0 to 1. Two-sided t -test: **** $P < 0.0001$. **i**, LYZ secretion assay for organoids differentiated in ENR+CD, treated with 10 μM SR11302 (AP-1 inhibitor) or 20 nM Cobimetinib (MEK inhibitor) for 6 d. Organoids were incubated in fresh basal media with or without 10 μM Cch for 3 h on day 6. All data were normalized to ATP abundance and standardized to the control in each experiment. Means and individual values are shown ($N = 5$), dotted line represents the control value (1). One-way ANOVA post-hoc Tukey's multiple comparisons test, ordered left to right, top to bottom: **** $P < 0.0001$, ** $P = 0.0014$, ** $P = 0.0055$, ** $P = 0.0035$, ** $P = 0.0085$, **** $P < 0.0001$. **j**, Proposed mechanism for XPO1 inhibition driving transcriptional changes manifesting as increased stress responses and reduced mitogen signalling, resulting in re-balanced cycling of stem cell fate decisions towards secretory Paneth cells and absorptive enterocytes.

XPO1-mediated effects on mitosis through association with Aurora kinases. We began by treating organoids along the ENR + CD differentiation course with SR11302, a small-molecule inhibitor of AP-1, to test whether AP-1 is critical to the SINE-induced stress response, both alone and in combination with KPT-330. We observe that SR11302 significantly decreases functional LYZ secretion at the end of the 6d differentiation, both in combination with KPT-330 and alone (Fig. 5i). This suggests that AP-1 signalling is a mediator of Paneth differentiation from ISCs.

We next tested whether p53 is a downstream mediator of XPO1 inhibition by repeating the above assay with two known p53 modulators: a p53 inhibitor pifithrin- α (PFT α) and p53 agonist serdemetan (serd.). Across a wide dose range, both p53 modulators tested did not alter Paneth cell differentiation—neither alone nor in combination with KPT-330—suggesting that the KPT-330 stress response is not dependent on extracellular signal-regulated kinases (ERK), but is further enhanced by ERK inhibition. Additionally, the non-exporter-related action of XPO1 during the cell cycle (which interacts with Aurora kinase) may further contribute to the observed pro-differentiation effect.

(previously shown to induce the quiescent ISC population⁴⁶), in combination with KPT-330. Cobimetinib alone did not significantly alter Paneth cell differentiation, but it synergized with KPT-330 (Fig. 5i) to increase Paneth cell differentiation. We next sought to test whether the regulation of the cell cycle via mitogen signalling may act as a downstream mediator following XPO1 inhibition. Inhibition of Cdk4/6 with palbociclib both alone and in combination with KPT-330 did not alter Paneth cell differentiation (Extended Data Fig. 5h), but inhibition of Aurora kinase B with ZM447439 did significantly increase Paneth cell differentiation (notably, ZM447439 was also a lower-effect-size hit in our primary screen) (Extended Data Fig. 5i). Combined, these experiments suggest that the SINE-induced stress response may be mediated by AP-1 but not p53, while suppression of mitogen signalling is not dependent on extracellular signal-regulated kinases (ERK), but is further enhanced by ERK inhibition. Additionally, the non-exporter-related action of XPO1 during the cell cycle (which interacts with Aurora kinase) may further contribute to the observed pro-differentiation effect.



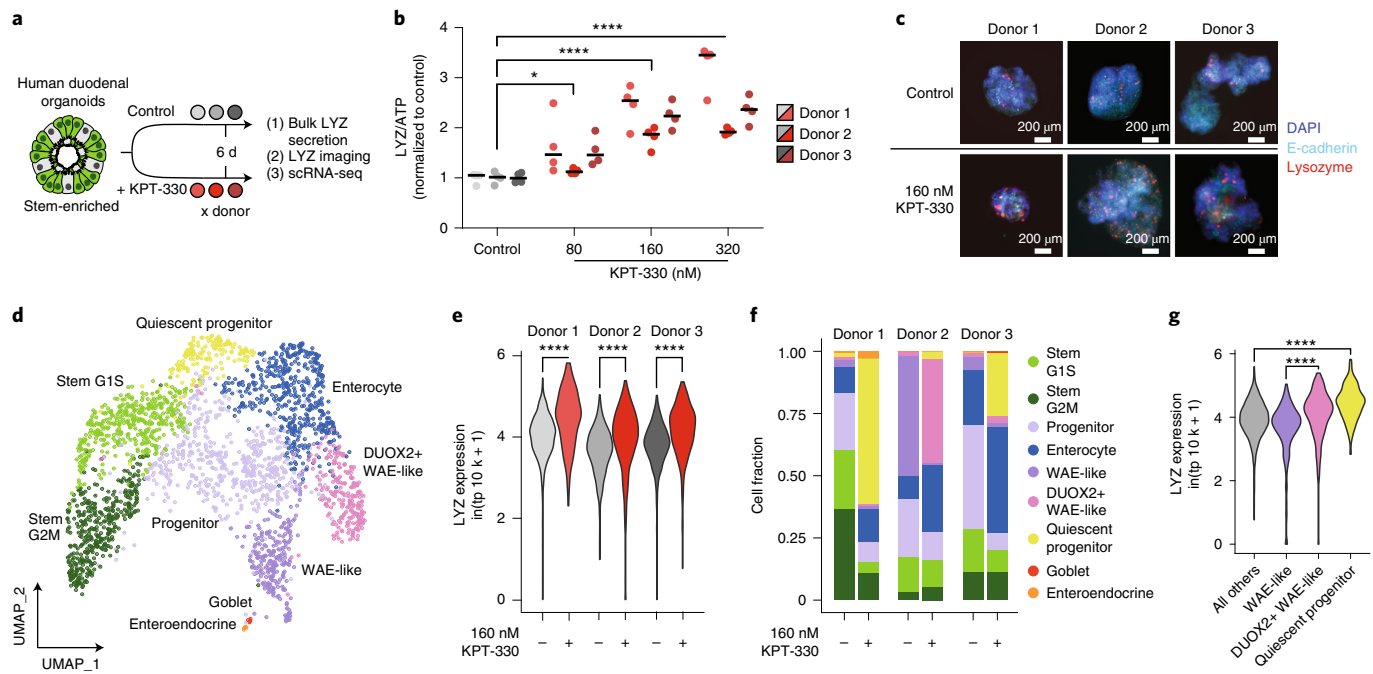


Fig. 6 | KPT-330-mediated XPO1 inhibition in human SI organoids has pro-differentiation effects that mirror those in the murine system. a,

Stem-enriched human small intestinal organoid differentiation in the presence and absence of KPT-330. Each circle represents a sample of organoids collected from a unique donor for a LYZ secretion assay, IF imaging and scRNA-seq over the 6 d time course. **b,** LYZ secretion assay for human organoids treated with increasing concentrations of KPT-330 for 6 d. Organoids were incubated in fresh basal media with $10 \mu\text{M}$ Cch for 3 h on day 6. All data were normalized to ATP abundance and standardized to the control in each experiment. Donor means and individual values are shown ($N=4$). One-way ANOVA post-hoc Dunnett's multiple comparisons test, ordered left to right: $*P=0.0114$, $****P<0.0001$. **c,** Representative immunofluorescence images of human organoids treated with 160 nM KPT-330 for 6 d; images from single experiment are shown. **d,** Organoid UMAP of all samples labelled by annotated cell type. **e,** Violin plot of scRNA-seq log-normalized (transcripts per 10,000 - tp10k) expression of LYZ in all cells, grouped by donor and split by KPT-330 treatment. Wilcoxon rank sum test, treated vs non-treated: $****P<0.0001$. **f,** Stacked bar chart for annotated cell type by cell type, grouped by donor and split by KPT-330 treatment. **g,** Violin plot of scRNA-seq log-normalized (transcripts per 10,000 - tp10k) expression of LYZ in all donors, grouped by cell type annotation. Wilcoxon rank sum test, DUOX2+ WAE-like vs WAE-like and quiescent progenitor vs all others: $****P<0.0001$.

In total, our analyses suggest that KPT-330-mediated XPO1 inhibition drives Paneth cell enrichment through the modulation of cell state within cycling ISCs (stem II/III). Further, this modulation includes a confluence of pan-epithelial stress response and suppression of mitogen signalling within stem II/III. We observe the cycling stem population becoming transiently quiescent, thereby favouring differentiation towards the Paneth and enterocyte lineages (the latter being a short-lived population relative to the former) over a more balanced transition to the mature lineages and the quiescent stem pool (stem I) (Fig. 5j).

KPT-330 mediates pro-barrier differentiation in human organoids. To extend our observations from the murine organoid system, we sought to examine how XPO1 inhibition via KPT-330 may affect human small intestinal stem cells by utilizing a stem-cell-enriched human small intestinal organoid model⁴⁷ (Methods). This model (as is the case for other reported human small intestinal organoid models) does not generate an appreciable mature Paneth cell population, probably owing to an absence of critical niche signalling factors. Thus, we sought to assess whether KPT-330 would alter patterns of stem cell differentiation (Fig. 6a), in a fashion consistent with our murine models. We performed a dose-response study with KPT-330 in a human-derived stem cell-enriched small intestinal organoid model from three unique duodenal donors and found that normalized LYZ secretion significantly increases with dose (Fig. 6b). At a single dose (160 nM KPT-330, equivalent to our murine organoid scRNA-seq study), we conducted IF imaging for LYZ and observed increased LYZ+ cell abundance (Fig. 6c). In both LYZ secretion and

imaging morphology, we see that there may be donor-dependent responses to KPT-330 treatment (note donor 1 appearing most responsive and donor 2 least).

To more completely explore the changes induced by KPT-330 in this human organoid model, and any donor associated effects, we again utilized scRNA-seq via Seq-Well S³. We performed a comparison between untreated and KPT-330-treated organoids from each donor over a 6 d differentiation, with each sample consisting of single cells from >1,000 organoids. The resulting dataset consists of 2,484 cells. UMI, percent mitochondrial and detected gene distributions are similar across samples, within acceptable quality bounds (genes >500, UMI <30,000, percent mitochondrial <35) (Extended Data Fig. 6a).

Following normalization, variable feature selection and principal component analysis (Methods), tiered Louvain clustering separated the data into 7 clusters with similar quality metrics (Extended Data Fig. 6b), which we manually annotated (Fig. 6d) on the basis of the expression of canonical marker genes of intestinal epithelial cell types (Extended Data Fig. 6d,e). To further determine the cellular identity of our 7 clusters, we used PROGENY to infer signalling pathway activity in each population (Extended Data Fig. 6e). The 7 clusters include 2 stem-like clusters (differing stages of cell cycle), 2 progenitor subsets, 2 clusters with features consistent with wound-associated epithelium (WAE-like), and a joint enterocyte, goblet and enteroendocrine cluster. The 2 WAE-like clusters (both marked by high expression of *CD55* and enriched signalling for hypoxia,^{48,49} one enriched in the known stress-associated antimicrobial gene *DUOX2*⁵⁰) have not been described previously in this

model but appear to be donor, rather than treatment, driven, as they were specifically enriched in donor 2 (Extended Data Fig. 6f,g). In donor 2, we observed a cystic-like morphology in some of the organoids, and the WAE-like populations may derive therefrom⁴⁸. Future work will be needed to substantiate the connection between these populations and organoid morphology.

On aggregate, KPT-330 increased LYZ expression (Fig. 6e) in a donor-dependent manner consistent with observations in our LYZ secretion assay and IF imaging. Furthermore, KPT-330 drives clear compositional changes, both pan-donor (decreases in cycling stem and progenitor populations, increases in quiescent progenitors and enterocytes) and donor-specific (shifts in WAE-like to DUOX2 + WAE-like) (Fig. 6f and Extended Data Fig. 6h). The populations uniquely enriched following KPT-330 treatment are also those with the highest levels of LYZ expression, including the quiescent progenitor and DUOX2 + WAE-like cells (Fig. 6g). *DUOX2* itself is a gene involved in innate barrier defence, suggesting that XPO1 inhibition via KPT-330 may induce expression of a subset of innate barrier defence genes. Finally, in addition to decreases in cycling populations and increases in innate defence gene expression and differentiation, we identified enrichment for NES-containing gene expression in the human system cycling stem populations as in the murine system. Moreover, following KPT-330 treatment, we saw the same signature compensatory increase in *XPO1* expression (Extended Data Fig. 6i). In total, the human intestinal organoid model used here demonstrated a clear effect of KPT-330 on the stem subsets as well as consistencies across species; nevertheless, its specific impact on human Paneth differentiation remains to be determined, given the original model insufficiency.

KPT-330 induces selective expansion of Paneth cells in vivo. We next sought to validate that our framework of biological target discovery in intestinal organoids can translate to the in vivo setting. On the basis of our understanding of KPT-330-mediated XPO1 inhibition in stem-enriched murine and human organoids, we hypothesized that SINE compounds may selectively enrich the epithelium for Paneth cells in vivo. Our findings in organoids suggest that SINE treatment is independent of the niche cues of Wnt and Notch (Extended Data Fig. 2b-f), and acts specifically on cycling stem cells (which are abundant in the epithelial crypts). While XPO1 inhibition may enrich Paneth cells, goblet cells and enterocytes, by virtue of the relatively long Paneth cell lifespan⁵¹ we would expect a longer-term accumulation of Paneth cells in vivo relative to goblet cells or enterocytes. Additionally, because XPO1 inhibition in organoids does not expand the stem cell pool but rather re-balances patterns of differentiation, we expect an increase in Paneth cell number following SINE treatment in vivo to be restricted to the spatially constrained non-hypertrophic crypt and proportional to the initial number of cycling progenitors. This suggests that in vivo increases in Paneth cell number may be modest, yet their biological effect may be significant, and therefore a particularly sensitive method of quantification is preferable.

Following a similar protocol as previously reported for SINE treatment in the context of cancer^{52–55}, KPT-330 was administered at a dose of 10 mg kg⁻¹ via oral gavage every other day over a 2-week span in C57BL/6 wild-type mice, and body weight was monitored for any clear toxicity. Within the treatment group, we observed significant weight loss indicative of toxicity (Extended Data Fig. 7a). Given animal weight loss on the standard chemotherapeutic dosage regimen, and additional evidence that sustained dosage of SINEs adversely impacts T cell populations⁵⁶, we sought to explore dosing regimens well below 10 mg kg⁻¹, to assess whether a pro-Paneth phenotype may exist below potential toxicities.

We repeated the 2-week study with oral gavage of KPT-330 every other day at doses corresponding to 50-fold (0.2 mg kg⁻¹), 200-fold (0.05 mg kg⁻¹) and 1,000-fold (0.01 mg kg⁻¹) decrease in

the 10 mg kg⁻¹ dose conventionally used in a cancer setting. Because Paneth cell number and quality are known to physiologically change along the length of the small intestine, and diseases associated with Paneth cells most frequently present distally⁵⁷, we sought to profile how XPO1 inhibition may differentially affect the proximal and distal small intestine. We tracked animal weight every other day and collected the proximal and distal thirds of the small intestine at day 14 for histological quantification of Paneth, stem and goblet populations (Fig. 7a). In this lower-dose regimen, we observe no significant changes in animal weight, suggesting that the doses are outside the gross toxicity range (Extended Data Fig. 7b). Paneth cells were counted within well-preserved crypts, with at least 30 crypts quantified per animal (representative images in Extended Data Fig. 7c), and the counts were averaged. Within this lower-dose regimen, we observe significant increases in Paneth cell abundance both in the proximal and distal small intestine at doses of 0.01 mg kg⁻¹, and proximally at 0.2 mg kg⁻¹ (Fig. 7b). To demonstrate the significance of this increase, we identified the 90th percentile abundance of Paneth cells per crypt in vehicle animals (4 per crypt proximally and 5 per crypt distally) (Extended Data Fig. 7d) and calculated the fraction of crypts with a greater number of Paneth cells than the 90th percentile cutoff for each KPT dose. In the proximal small intestine, 0.2 mg kg⁻¹ nearly tripled this fraction (15.5% vs vehicle 5.8%), while in the distal small intestine, 0.01 mg kg⁻¹ more than doubled this fraction (27.9% vs 12.2%). We additionally quantified the abundance of *Olfm4+* stem cells as well as PAS+ goblet cells within the same animals to ascertain whether the effect of SINE treatment was restricted to the Paneth cell compartment (representative images in Extended Data Fig. 7e,f). We observe a significant increase in *Olfm4+* stem cells within the distal small intestine (SI) at doses of 0.01 mg kg⁻¹, corresponding to the group with the greatest increase in Paneth cells (Fig. 7d), suggesting a potential expansion of the stem cell niche commensurate with increased Paneth cell abundance. We did not identify any significant changes in the developmentally related goblet cell population (Fig. 7e). In total, these data suggest that SINE treatment may be a meaningful approach to specifically increase Paneth cell abundance in vivo, and further validates our framework for using models of organoid differentiation in small-molecule screening.

Discussion

Here we demonstrate that by employing phenotypic small-molecule screening in a physiologically motivated organoid model, we can uncover biological targets and clinically relevant small molecules that translate to in vivo and inform cross-species (mouse to human) tissue stem cell biology, without previous knowledge of that biological target's function in vivo. Further, this approach to small-molecule phenotypic screening enables a specific, functional readout in a dynamic and heterogeneous organoid model, and may be suited to uncover targets not readily amenable to genetic perturbation (for example *Xpo1*, a gene essential to cell survival through its role in mitosis). Our approach provides perturbation capacity nearly two orders of magnitude greater than existing examples of non-genetic perturbations in organoid models, thereby enabling screens within the space of annotated small-molecule libraries and empowering biological target discovery.

By using a model that focuses on differentiation to a specific lineage (the Paneth cell), we are able to resolve a pathway and compounds that direct ISC fate decisions to drive subtle but significant effects on the in vivo tissue. We identify a series of compounds known to inhibit the nuclear exporter XPO1, acting on cycling ISCs by inducing a programme of stress response and decreased mitogen signalling. This ISC response re-balances self-renewal and differentiation towards Paneth cell differentiation. Recent work on mitogen and stress response control of re-entry into the cell cycle may provide context on the necessity of overlap of these two responses

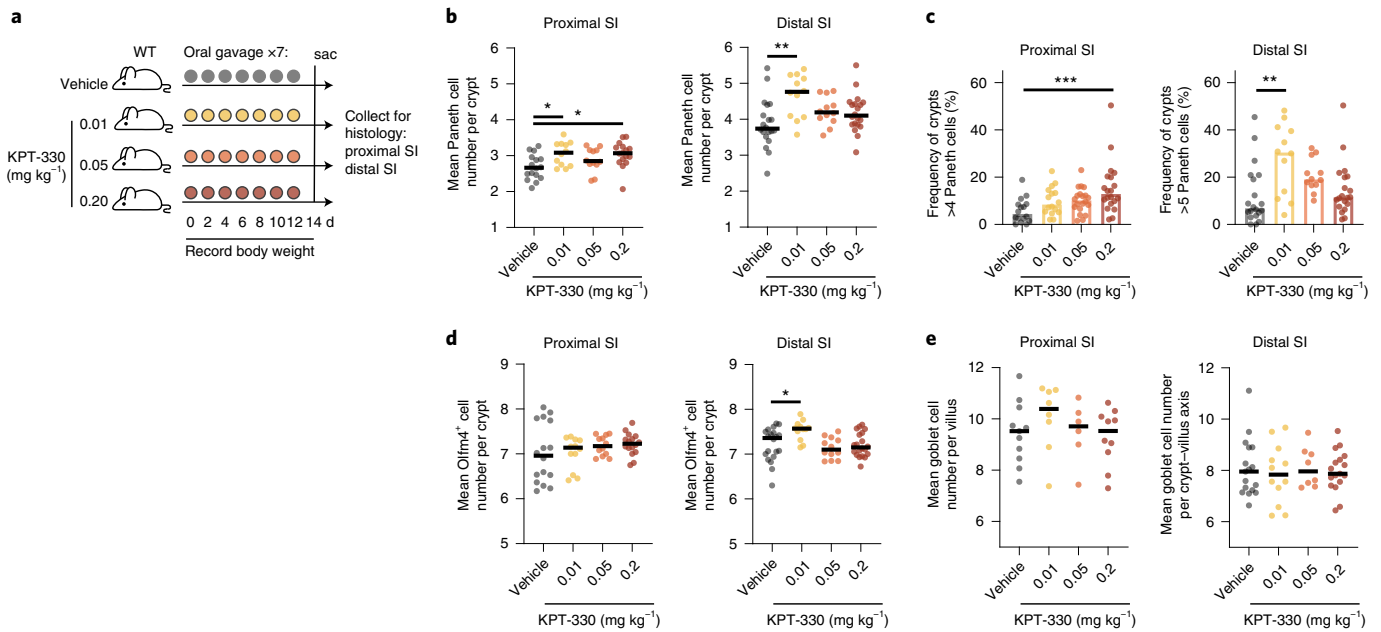


Fig. 7 | XPO1 inhibition with KPT-330 increases Paneth cell number in vivo. **a**, Design for in vivo oral gavage of KPT-330 in wild-type (WT) C57BL/6 mice. **b**, Mean Paneth cell number per crypt in proximal or distal third of small intestine, quantified by blinded histological counting. Means and individual values (representing mean of ≥ 30 crypt counts per biological replicate) are shown. $N=16$ (vehicle and 0.2 mg kg⁻¹, proximal), $N=20$ (vehicle and 0.2 mg kg⁻¹, distal), $N=12$ (0.01 and 0.05 mg kg⁻¹, proximal and distal). One-way ANOVA post-hoc Dunnett's multiple comparisons test, ordered left to right: * $P=0.0175$, * $P=0.0135$, ** $P=0.0012$. **c**, Frequency of crypts with 4 or more (proximal third) or 5 or more (distal third) Paneth cells per animal across KPT-330 treatment groups, from blinded histological counts. Means and individual values (representing mean of ≥ 30 crypt counts per biological replicate) are shown. $N=16$ (vehicle and 0.2 mg kg⁻¹, proximal), $N=20$ (vehicle and 0.2 mg kg⁻¹, distal), $N=12$ (0.01 and 0.05 mg kg⁻¹, proximal and distal). One-way ANOVA post-hoc Dunnett's multiple comparisons test: *** $P=0.0007$, ** $P<0.0017$. **d**, Mean Olfm4⁺ stem cell number per crypt in proximal or distal third of small intestine, quantified by blinded histological counting. Means and individual values (representing mean of ≥ 17 crypt counts per biological replicate) are shown. $N=16$ (vehicle and 0.2 mg kg⁻¹, proximal), $N=20$ (vehicle and 0.2 mg kg⁻¹, distal), $N=12$ (0.01 and 0.05 mg kg⁻¹, proximal and distal). One-way ANOVA post-hoc Dunnett's multiple comparisons test: * $P=0.0112$. **e**, Mean PAS⁺ goblet cell number per villus in proximal or distal third of small intestine, quantified by blinded histological counting. Means and individual values (representing mean of ≥ 15 villus counts per biological replicate) are shown. $N=11$, 8, 6, 10 (vehicle, 0.01, 0.05, 0.2 mg kg⁻¹, proximal), $N=17$, 12, 8, 17 (vehicle, 0.01, 0.05, 0.2 mg kg⁻¹, distal).

in directing decisions of fate commitment⁵⁸. Transitions between quiescence and proliferation within the ISC niche have roles in tissue homeostasis and regeneration. Quiescent cells serve as reserve populations that upon injury of cycling stem cells, will re-establish progenitors and maintain homeostatic tissue regeneration^{59,60}. Further, a transient quiescent ISC state facilitates secretory enteroendocrine cell differentiation⁴⁶, and may explain why we see synergistic Paneth cell enrichment with a combination of ERK and XPO1 inhibition. Furthermore, ERK inhibition may affect differentiation by either suppression of enterocyte differentiation⁶¹ or augmentation of Wnt signalling⁶². Additionally, we see that the pan-epithelial stress response induced by KPT-330-mediated XPO1 inhibition in vitro involves the AP-1 pathway, which also appears to play a role in Paneth differentiation and may be mediated via transcriptional changes in Atf3. In vivo, Atf3 is implicated in the regulation of stress responses in disease of the barrier tissue^{42,63}, where XPO1 may be one way to access these observed responses for therapeutic use.

Critical aspects from our murine organoid study appear to carry over to the human organoid model. We observe that KPT-330-mediated XPO1 inhibition clearly suppresses cell cycle activity and encourages differentiation and expression of innate defence genes (*LYZ*, *DUOX2*). It appears that KPT-330-mediated XPO1 inhibition induces a unique quiescent progenitor population in the human organoids, which may have resemblance to a pro-secretory progenitor known to be important in the murine model⁴⁶. It is also clear that because the human model lacks Paneth cells, direct observation of differentiation and further screening for modulators of Paneth cells is limited. Future refinement of the human organoid

model would empower more definitive conclusions about XPO1's role in human Paneth cell development. Finally, understanding drivers of donor-to-donor variability in the human setting also poses a challenge for the field moving forward.

While we have demonstrated that KPT-330-mediated XPO1 inhibition in vivo significantly increases the abundance of Paneth cells within the small intestinal crypts, we believe there are key mediators that may explain heterogeneity of biological potency along the small intestine, and may be investigated to enhance effect in future studies. Our in vitro work suggests that KPT-330-mediated XPO1 inhibition induces differentiation, we would therefore not expect a gross remodeling of crypt architecture, which is an inherently constrained space in vivo, having an average of 3.5 to 4 Paneth cells, and thus would anticipate that increases in Paneth cell number would be modest and in line with tissue microarchitecture along the gastrointestinal tract. In fact, we feel that the increase of an additional 0.5–1 Paneth cell per crypt that we observe in vivo is in favour of the specific and significant effect of the identified agent. We further note that this demonstration specifically increases Paneth abundance in vivo without inducing crypt hypertrophy or targeting potentially oncogenic pathways, avoiding concerns with previous agents shown to modulate in vivo Paneth abundance (Wnt activators and Notch inhibitors).

We also strongly believe that future study outside the scope of the present work is warranted to better elucidate the role of XPO1 and XPO1 inhibitors in modulating adult epithelial stem cell fate commitment. Our present evidence for XPO1's role in mediating intestinal stem cell differentiation in a pro-Paneth manner is known

only by chemical inhibition, and there may exist yet undescribed off-target effects of the inhibitors tested here that could inform the observations leading to our proposed mechanism. Future work to explore the biological role of XPO1 in intestinal stem cell differentiation through genetic means, such as the use of an XPO1 C528S mutant⁶⁴ in an organoid or in vivo, are critical next steps to confirming a mechanistic role for XPO1. Additionally, as our knowledge of the in vivo stem cell niche improves, organoid models can be refined in an iterative fashion, further enhancing model fidelity and increasing the probability of compound translation from in vitro to in vivo conditions.

This approach – employing a physiologically motivated set of cues to modulate ISC differentiation and layering on a screen for unreported regulators of that differentiation at scale – may be further applied both within the small intestine and more broadly across adult barrier tissues to modulate tissue composition through unreported molecular targets and associated small molecules. For example, this same framework may be applied in the context of enteroendocrine cell development within the small intestine to explore ways in which hormone secretion, including that of Glp-1, may be modulated or in the context of goblet cell development to identify agents that may transiently enhance mucus production. While establishing the appropriate model and screening assay for a study of enteroendocrine or goblet differentiation is not trivial, it should be possible based on the approach we have demonstrated here. Additionally, a small-molecule approach may offer the benefit of transient control of tissue composition, which may be reversed with removal of the agent. Overall, we provide a framework to construct organoid models of lineage-specific differentiation that can uncover pathways regulating differentiation and reveal compounds controlling barrier tissue composition.

Methods

Murine crypt isolation and organoid culture. Small intestinal crypts were isolated under animal protocols approved by the Massachusetts Institute of Technology (MIT) Committee on Animal Care (CAC). Proximal and/or distal small intestines were isolated from wild-type C57BL/6 mice of both sexes, aged between 1 and 6 months in all experiments. Small intestinal crypts were isolated as previously described²³. Briefly, the small intestine was collected, opened longitudinally and washed with ice-cold Dulbecco's phosphate buffered saline without calcium chloride and magnesium chloride (PBS0) (Sigma-Aldrich) to clear the luminal contents. The tissue was cut into 2–4 mm pieces with scissors and washed repeatedly by gently pipetting the fragments using a 10 ml pipette until the supernatant was clear. Fragments were rocked on ice with crypt isolation buffer (2 mM EDTA in PBS0; Life Technologies) for 30 min. After isolation buffer was removed, fragments were washed with cold PBS0 by pipetting up and down to release the crypts. Crypt-containing fractions were combined, passed through a 70 µm cell strainer (BD Bioscience), and centrifuged at 300 r.c.f. for 5 min. The cell pellet was resuspended in basal culture medium (2 mM GlutaMAX (Thermo Fisher) and 10 mM HEPES (Life Technologies) in advanced DMEM/F12 (Invitrogen)) and centrifuged at 200 r.c.f. for 2 min to remove single cells. Crypts were then cultured in a Matrigel culture system (described below) in small intestinal crypt medium (100X N2 supplement (Life Technologies), 100X B27 supplement (Life Technologies), 1 mM *N*-acetyl-L-cysteine (Sigma-Aldrich) in basal culture medium) supplemented with differentiation factors at 37 °C with 5% CO₂. Penicillin/streptomycin (100X) was added for the first 4 d of culture post-isolation only.

Small intestinal crypts were cultured as previously described²³. Briefly, crypts were resuspended in basal culture medium at a 1:1 ratio with Corning Matrigel membrane matrix–GFR (Thermo Fisher) and plated at the centre of each well of 24-well plates. Following Matrigel polymerization, 500 µl of crypt culture medium (ENR + CV) containing growth factors EGF (50 ng ml⁻¹, Life Technologies), Noggin (100 ng ml⁻¹, PeproTech) and R-spondin 1 (500 ng ml⁻¹, PeproTech) and small molecules CHIR99021 (3 µM, LC Laboratories or Selleck Chem) and valproic acid (1 mM, Sigma-Aldrich) was added to each well. ROCK inhibitor Y-27632 (10 µM, R&D Systems) was added for the first 2 d of ISC culture only. The cell culture medium was changed every other day. After 4 d of culture, crypt organoids were expanded as and enriched for ISCs under the ENR + CV condition. Expanding ISCs were passaged every 4–6 d in the ENR + CV condition.

After 2–6 d of culture under ENR + CV condition, ISCs were differentiated to Paneth cells. Briefly, ISC culture gel and medium were homogenized via mechanical disruption and centrifuged at 300 r.c.f. for 3 min at 4 °C. The

supernatant was removed and the pellet resuspended in basal culture medium repeatedly until the cloudy Matrigel was almost gone. On the last repeat, the pellet was resuspended in basal culture medium, the number of organoids counted, and the suspension centrifuged at 100 r.c.f. for 1 min at 4 °C. The cell pellet was resuspended in basal culture medium at a 1:1 ratio with Matrigel and plated at the centre of each well of 24-well plates (~100–250 organoids per well). Following Matrigel polymerization, 500 µl of crypt culture medium (ENR + CV) was added to each well. The cell culture medium was changed every 2–4 d depending on seeding density.

Human crypt isolation and organoid culture. Excess surgical tissue samples from adult human duodenum were collected for organoid culture in accordance with Massachusetts General Hospital Institutional Review Board (IRB) guidance under Mass General Brigham Protocol 2010P000632. De-identified human donor tissue was collected following medically indicated bulk surgical resection via MGH Pathology as excess tissue. Donors of both sexes, aged between 58–74 years, presented with pathologies unrelated to the duodenum. Crypts were isolated from bulk resections as follows. Bulk resections were cut into approximately 0.25 cm sections from the epithelial surface, and washed in PBS0 repeatedly by gently pipetting the fragments using a 10 ml pipette until the supernatant was clear. Fragments were rocked on ice with crypt isolation buffer (10 mM EDTA, 10 mM HEPES, 2% FCS in PBS0) for 30 min. After isolation buffer was removed, fragments were washed with cold PBS0 by vigorous shaking to release the crypts. This process was repeated with reserved crypt-laden supernatant fractions 4–6 times or until supernatant was free of intact crypts (visual inspection). Crypt-containing fractions were combined, passed through a 100 µm cell strainer (BD Bioscience), and centrifuged at 300 r.c.f. for 5 min. The crypt pellet was resuspended in basal culture medium (2 mM GlutaMAX (Thermo Fisher) and 10 mM HEPES (Life Technologies) in advanced DMEM/F12 (Invitrogen)) and centrifuged at 200 r.c.f. for 2 min to remove single cells. Crypts were then cultured in a Matrigel culture system (described previously). Organoids were cultured and passaged as described for murine organoids every 6–8 d in Matrigel domes with established media conditions meant to recapitulate a stem cell-enriched condition²⁷. Organoid culture media contained recombinant EGF (Thermo Fisher), FGF2 (Thermo Fisher), IGF1 (PeproTech), Gastrin (Sigma Millipore) and TGF- β inhibitor A83-01 (Tocris Bioscience) with 50% conditioned medium of L-cell line secreting Wnt3a, R-spondin3 and Noggin (L-WRN CM) supplemented with 10 µmol l⁻¹ Y-27632 (Tocris Bioscience). L-WRN CM was prepared from L-WRN (ATCC; CRL-3276) as described previously⁶⁵. L-WRN (50%) is a 1:1 mixture of 100% L-WRN and primary culture medium. Primary culture media consist of advanced DMEM/F12, penicillin/streptomycin, GlutaMAX (all from Thermo Fisher), and FBS (20%). Organoid samples grown in culture over varying periods were either maintained and passaged or treated with 160 nM KPT-330 for 6 d before assay, with media changes every other day.

High-throughput screening. For 384-well plate high-throughput screening, ISC-enriched organoids were passaged and split into single cells with TyrpLE (Thermo Fisher) and cultured for 2–3 d in ENR + CVY (Y: Y-27632 at 10 µM) before transfer to a '2.5D' 384-well plate culture system. To prepare for '2.5D' plating, cell-laden Matrigel and media were homogenized via mechanical disruption and centrifuged at 300 r.c.f. for 3 min at 4 °C. The supernatant was removed and the pellet washed and spun in basal culture medium repeatedly until the cloudy Matrigel above the cell pellet was gone. On the final wash, the pellet was resuspended in basal culture medium, the number of organoids counted, and the cell pellet resuspended in ENR + CD medium at ~7 clusters per µl. Plates (384-well) were first filled with 10 µl 70% Matrigel (30% basal media) coating in each well using a Tecan Evo 150 liquid handling deck, and allowed to gel at 37 °C for 5 min. Then 30 µl of cell-laden media was plated at the centre of each well of 384-well plates with the liquid handler, and the plates were spun down at 100 r.c.f. for 2 min to embed organoids on the Matrigel surface. Compound libraries were pinned into prepped cell plates using 50 nl pins into 30 µl media per well. Cells were cultured at 37 °C with 5% CO₂ for 6 d in ENR + CD medium supplemented with the tested compounds, with media change at 3 d. On day 6, lysozyme secretion and cell viability were assessed using lysozyme assay kit (EnzChek) and CellTiter-Glo 3D (CTG 3D) cell viability assay (Promega), respectively, according to the manufacturers' protocols. Briefly, screen plates were washed 3x with FluoroBrite basal media (2 mM GlutaMAX and 10 mM HEPES in FluoroBrite DMEM (Thermo Fisher)) using a BioTek 406 plate washer with 10 min incubations, followed by a 1 min centrifugation at 200 r.c.f. to settle media between washes. After removal of the third wash, 30 µl of non-stimulated FluoroBrite basal media was added to each screen well using a Tecan Evo 150 liquid handling deck from a non-stimulated treatment master plate, and plates were incubated for 30 min at 37 °C. After 30 min, the top 15 µl of media from each well of the screen plate was transferred to a non-stimulated LYZ assay plate containing 15 µl of 20X DQ LYZ assay working solution using a Tecan Evo 150 liquid handling deck. The non-stimulated LYZ assay plate was covered, shaken for 10 min, incubated for 50 min at 37 °C, then fluorescence measured (shaken for 10 s; 494 nm/518 nm) using a Tecan M1000 plate reader. After media transfer to the non-stimulated LYZ assay plate, the remaining media were removed from the screen plate and 30 µl of

stimulated FluoroBrite basal media (supplemented with 10 μM CCh) was added to each screen well using a Tecan Evo 150 liquid handling deck from a stimulated treatment master plate, and plates were incubated for 30 min at 37 $^{\circ}\text{C}$. After 30 min, the top 15 μl of media from each well of the screen plate was transferred to a stimulated LYZ assay plate containing 15 μl of 20X DQ LYZ assay working solution using a Tecan Evo 150 liquid handling deck. The stimulated LYZ assay plate was covered, shaken for 10 min, incubated for 50 min at 37 $^{\circ}\text{C}$, then fluorescence measured (shaken for 10 s; 494 nm/518 nm) using a Tecan M1000 plate reader. Finally, 8 μl of CTG 3D was added to each well of the screen plate, which was shaken for 30 min at room temperature, then luminescence read (shaken for 10 s; integration time 0.5–1 s) to measure ATP.

Primary screens were performed using the Target-Selective Inhibitor Library (Selleck Chem). Assays were performed in triplicate using 4 compound concentrations (0.08, 0.4, 2 and 10 μM).

Screen analysis. Analysis of all screen results was performed in R. Results (excel or.csv files) were converted into a data frame containing raw assay measurements corresponding to metadata for plate position, treatments, doses, cell type and stimulation. Raw values were \log_{10} transformed, then a locally estimated scatterplot smoothing (LOESS) normalization was applied to each plate and assay to remove systematic error and column/row/edge effects using the formula:⁴⁶

$$\hat{x}_{ij} = x_{ij} - (\text{loess.fit}_{ij} - \text{median}(\text{loess.fit}_{ij})), \quad (1)$$

where \hat{x}_{ij} is the LOESS fit result, x_{ij} is the \log_{10} transformed value at row i and column j , and loess.fit_{ij} is the value from LOESS smoothed data at row i and column j calculated using R loess function with span 1.

Following LOESS normalization, a plate-wise fold change (FC) calculation was performed on each well to normalize plates across the experiment. This was calculated by subtracting the median of the plate (as control) from the LOESS normalized values:

$$\text{FC}_{ij} = \hat{x}_{ij} - \text{median}(\hat{x}_{ij}). \quad (2)$$

Replicate strictly standardized mean difference (SSMD) was used to determine the statistical effect size of each treatment in each assay (treatment and dose grouped by replicate, $n=3$) relative to the plate, using the formula for the robust uniformly minimal variance unbiased estimate (UMVUE):⁴⁷

$$\text{SSMD} = \frac{\Gamma(\frac{n-1}{2})}{\Gamma(\frac{n-2}{2})} \sqrt{\frac{2}{n-1}} \frac{\bar{d}_i}{\sqrt{w_i s_i^2 + w_0 s_0^2}}, \quad (3)$$

where \bar{d}_i and s_i are respectively the sample mean and standard deviation of d_{ij} s where d_{ij} is the FC for the i th treatment on the j th plate. $\Gamma(\cdot)$ is a gamma function. s_0^2 is an adjustment factor equal to the median of all s_i^2 s to provide a more stable estimate of variance. w_i and w_0 are weights equal to 0.5 with the constraint of $w_i + w_0 = 1$. n is the replicate number.

Mean FC (the arithmetic mean of all samples grouped by treatment and dose across replicates) was used to determine the z -score for each treatment and dose with the formula:

$$z = \frac{\text{meanFC}}{\text{SD}_{\text{pop}}}, \quad (4)$$

where SD_{pop} is the standard deviation of all mean FCs.

All calculated statistics were combined in one finalized data table and exported as a.csv file for hit identification. A primary screen 'hit' was defined as having SSMDs for both LYZ assays greater than the optimal critical value ($\beta_{\alpha_1} = 0.997$) and being in the top 10% of a normal distribution of FC values for both assays with a z -score cutoff >1.282 . β_{α_1} was determined by minimizing the false positive (FPL) and false negative (FNL) levels for upregulation SSMD-based decisions by solving for the intersection of the formulas:⁴⁷

$$F_{t(n-1, \sqrt{n}\beta_2)} \left(\frac{\beta_{\alpha_1}}{k} \right) = 1 - \text{FPL} \quad (5)$$

and

$$\text{FNL} = F_{t(n-1, \sqrt{n}\beta_1)} \left(\frac{\beta_{\alpha_1}}{k} \right), \quad (6)$$

where

$$k = \sqrt{\frac{1}{n}} \quad (7)$$

and $F_{t(n-1, \sqrt{n}\beta)}$ is the cumulative distribution function of non-central t -distribution $t(n-1, \sqrt{n}\beta)$, n is the number of replicates, β_2 is an SSMD bound for FPL of 0.25 (at least very weak effect) and β_1 is an SSMD bound for FNL of 3 (at least strong effect).

Hit treatments were thus selected to have a well-powered statistical effect size as well as a strong biological effect size. Optimal dose per hit treatment was determined by SSMD for both LYZ assays.

Secondary lysozyme secretion assay screen. Confirmatory secondary screening with primary hits was performed using the above 384-well plate method. The screen was conducted with 4-plate replicates with a base media of ENR+CD. Media was supplemented with compound at day 0 and day 3 ($n=8$ well replicates per dose) at 4 different doses: twofold above, twofold below and fourfold below the optimal final dose for each respective treatment. Additionally, each plate carried a large number of ENR+DMSO or ENR+CD+DMSO (vehicle) control wells ($n=100$ for ATP, and $n=25$ for LYZ.NS and LYZ.S) for robust normalization. ATP, non-stimulated lysozyme activity and CCh-stimulated lysozyme activity were again measured and the collected data were again processed in a custom R-script per primary screen, with slight modification. Values were \log_{10} transformed, and a plate-wise FC was calculated for each well on the basis of the median value of ENR+CD+DMSO (vehicle) control wells to normalize plate to plate variability. The following formula was used:

$$\text{FC}_{ij} = x_{ij} - \text{median}(x_{\text{POS}}), \quad (8)$$

where x_{ij} is the \log_{10} transformed value at row i and column j , and x_{POS} are the values of the positive control wells. For the ATP assay, all vehicle-only wells were used as the control. For the LYZ.NS assay, non-stimulated vehicle-only wells were used. For the LYZ.S assay, vehicle-only wells that were non-stimulated in the LYZ.NS assay then stimulated in the LYZ.S assay were used.

Once normalized, the replicate SSMD was calculated using equation (3) to quantify statistical effect size, with 8 replicate differences taken relative to the respective plate ENR+DMSO or ENR+CD+DMSO median value. A primary hit was considered validated when SSMDs for both LYZ assays were greater than the optimal critical value (β_{α_1}) of 0.889. β_{α_1} was determined using equation (5), with an FPL error of 0.05 for a more stringent cutoff; FNL was not considered. Optimal doses were chosen for treatments with multiple validated doses by taking the most potent (highest mean fold change relative to ENR+CD control) dose in both LYZ assays.

Lysozyme secretion assay. ISC-enriched organoids in 3D Matrigel culture were passaged to a 48- or 96-well plate and cultured with ENR or ENR+CD media containing DMSO or each drug for 6 d. DMSO- or drug-containing media were changed every other day. On day 6, cells were washed with basal media twice and treated with basal media with or without 10 μM carbachol for 3 h in a CO_2 incubator at 37 $^{\circ}\text{C}$. Conditioned media was collected and used for lysozyme assay (Thermo Fisher, E-22013) following the manufacturer's instruction. The fluorescence was measured using excitation/emission of 485/530 nm. CTG 3D Reagent was added afterward, and the cell culture plate was incubated on an orbital shaker at RT for 30 min to induce cell lysis and to stabilize the luminescent signal. The solution was replaced to a 96-well white microplate, and luminescent signals were measured by a microplate reader (infinite M200, Tecan). The standard curve was prepared by diluting recombinant ATP (Promega, P1132). For both assays, a polynomial cubic curve was fitted to a set of standard data, and each sample value was calculated on the Microsoft Excel.

Flow cytometry. ISC-enriched organoids in 3D Matrigel culture were passaged to a 24- or 48-well plate and induced to differentiate for 6 d by ENR+CD media containing DMSO or each drug indicated in the figures. DMSO- or drug-containing media were changed every other day. On day 6, cells were washed twice with basal media, then collected from Matrigel by mechanical disruption in TrypLE Express (Thermo Fisher, 12605010) to remove Matrigel and dissociate organoids to single cells. After vigorous pipetting and incubation at 37 $^{\circ}\text{C}$ for 15 min, the cell solution was diluted twice with basal media and centrifuged at 300 r.c.f. for 3 min. The cell pellet was resuspended in FACS buffer (PBS containing 2% FBS) and replaced into a 96-well clear round-bottom ultra-low attachment microplate (Corning, 7007). The cell solution was centrifuged again at 300 r.c.f. for 3 min at 4 $^{\circ}\text{C}$ to pellet the cells. Cells were stained with Zombie-violet dye (BioLegend, 423113, 1:100) at 100X for viability staining for 20 min at r.t. in the dark. After centrifugation for 3 min at 300 r.c.f., cells were fixed in fixation buffer (FACS buffer containing 1% formaldehyde (Thermo Fisher, 28906)) for 15 min on ice in the dark. Cells were centrifuged again for 3 min at 300 r.c.f. and blocked with staining buffer (FACS buffer containing 0.5% Tween 20 (Sigma, P2287)) for 15 min at r.t. in the dark. Cells pelleted by centrifugation for 3 min at 300 r.c.f. were stained with FITC-conjugated anti-lysozyme antibody (Dako, F0372, 1:100) and APC-conjugated anti-CD24 antibody (Biolegend, 138505, 1:100) at 100X for 45 min at r.t. in the dark. The cell pellet was washed once with FACS buffer, resuspended in FACS buffer and filtered through a 5 ml test tube with cell strainer snap cap (Corning, 352235). Flow cytometry was performed using an LSR Fortessa (BD; Koch Institute Flow Cytometry Core at MIT). Flow cytometry data were analysed using FlowJo X v10.6.1 software.

Western blotting. Organoid-containing gel was homogenized in basal medium and centrifuged at 300 r.c.f. for 3 min. The organoid pellet was lysed with ice-cold

Pierce IP lysis buffer (Thermo Fisher, 87787) containing EDTA-free Halt protease inhibitor cocktail (Thermo Fisher, 87785) and incubated on ice for 20 min. The lysate was centrifuged at 17,000 r.c.f. for 10 min, and the supernatant was combined with NuPAGE LDS sample buffer (Thermo Fisher, NP0007). Protein concentration was determined by Pierce 660 nm protein assay (Thermo Fisher, 22660) and normalized to the lowest concentration among each sample set. Samples were incubated at 70°C for 10 min and resolved by SDS-PAGE using NuPAGE 4–12% Bis-Tris protein gels (Thermo Fisher), followed by electroblotting onto Immun-Blot PVDF Membrane (Biorad, 1620174) using Criterion blotter with plate electrodes (Biorad, 1704070). The membranes were blocked with 2% blotting-grade blocker (Biorad, 1706404) in TBS-T (25 mM Tris-HCl, 140 mM NaCl, 3 mM potassium chloride and 0.1% Tween 20) and then probed with appropriate antibodies, diluted in TBS-T containing 2% BSA (Sigma, A7906) and 0.05% sodium azide (Sigma, 71289). The primary antibody against lysozyme was purchased from Abcam (ab108508 1:2000). HRP-linked anti-rabbit IgG antibodies were purchased from Cell Signalling Technology (7074, 1:2,000). Chemiluminescent signals were detected by LAS4000 (GE Healthcare) using Amersham ECL Select western blotting detection reagent (GE Healthcare, 45-000-999), and total protein signals were obtained by Odyssey imaging system (LI-COR Biosciences) using REVERT total protein stain kit (LI-COR Biosciences, 926-11010).

Immunofluorescent imaging. For immunofluorescence staining of organoids, intestinal organoids in Matrigel were fixed with 4% paraformaldehyde, then transferred to centrifuge tubes. After washing with PBS, the isolated organoids were permeabilized with 1% Triton X, followed by incubation with blocking buffer (1% BSA + 3% Donkey Serum + 0.2% Triton X in PBS) at r.t. The organoids were then stained with primary antibodies and fluorescent dye-labelled secondary antibodies, as well as with 4',6-diamidino-2-phenylindole (DAPI). Slides were covered with VECTASHIELD mounting media (VECTOR). The following primary and secondary antibodies were used for the staining: rabbit anti-lysozyme (Thermo Fisher, RB-372-A, 1:1,000), rat anti-E-cadherin (Thermo Fisher, 13-1900, 1:1,000), and Alexa Fluor 488 and 568 secondary antibodies (Thermo Fisher A21208, A10042, 1:1,000). Images were acquired with a confocal laser scanning microscope (Nikon Eclipse 90i) with the following acquisition settings: DAPI exposure time 2 ms, contrast gain 0; FITC (for E-cadherin) exposure time 39 ms, contrast gain 0; TRITC (for lysozyme) exposure time 30 ms, contrast gain 0. For the analysis of lysozyme+ cells per organoid area, the number of counted lysozyme+ cells were normalized to the measured organoid surface area. Fiji v2.0 was used for quantification of lysozyme+ cells.

Animal study. All animal studies were performed under animal protocols approved by the MIT CAC. Wild-type C57BL/6Ncrl male mice (8–10-week-old, 027) were purchased from Charles River. Mice were housed under 12 h light/dark cycle, provided food and water ad libitum, and kept in a 20–22°C and 30–70% humidity environment. KPT-330 (0.01, 0.05, 0.2 or 10 mg kg⁻¹) were injected orally using a disposable gavage needle (Cadence Science, 9921) at 10 μl g⁻¹ weight. KPT-330 was dissolved in DMSO initially and further diluted in sterile PBS containing Pluronic F-68 non-ionic surfactant (Gibco, 24040032) and polyvinylpyrrolidone (PVP, Alfa Aesar, A14315, average M.W. 58,000); the final concentration of DMSO is 2%, Pluronic 0.5% and PVP 0.5%. KPT-330 was administered every other day for 2 weeks, for a total of 7 injections (days 0, 2, 4, 6, 8, 10, 12), and mice were killed at day 14.

Histology. The SI was collected from mice and divided into three parts. Only proximal and distal SI were kept in PBS, and medial SI was discarded. Each SI was opened longitudinally and washed in PBS. SI was rolled using the Swiss-rolling technique and incubated in 10% neutral buffered formalin (VWR, 10790-714) for 24 h at r.t. Fixed tissues were embedded in paraffin and 4 μm sections were mounted on slides. For immunohistochemistry, slides were deparaffinized, antigen retrieved using heat-induced epitope retrieval at 97°C for 20 min with citrate buffer pH 6, and probed with appropriate antibodies, followed by 3,3'-Diaminobenzidine (DAB) staining. An antibody against lysozyme was purchased from Abcam (ab108508, 1:2,000), Ki67 from BD Biosciences (550609 1:40) and Olfm4 from Cell Signalling Technology (39141, 1:1,000). For McManus periodic acid Schiff (PAS) reaction, slides were deparaffinized, oxidized in periodic acid and stained with Schiff reagent (Poly Scientific, s272), followed by counterstaining with Harris hematoxylin. Slides were scanned using an Aperio slide scanner (Leica) and cells were counted on an Aperio eSlide Manager. Slides were blinded and randomized before counting, and all cell types were counted in all well-preserved crypts along the longitudinal crypt-villus axis (Paneth cell, ≥30 crypts; Olfm4+ cell, ≥17 crypts; goblet cell, ≥15 villi, per sample). For the goblet cell images, the samples that included <15 well-preserved crypt-villus axes were excluded, which was predetermined.

Murine and human scRNA-seq and alignment. A single-cell suspension was obtained from murine organoids cultured under either ENR+CD or ENR+CD+160 nM KPT-330 for the differentiation time course as detailed in Fig. 2a, or human organoids treated with 160 nM KPT-330 as detailed in Fig. 6a. For

both, organoids at each sampling were collected from 4–6 pooled Matrigel domes, totalling >1,000 organoids per sample. Excess Matrigel was removed per previously described washing protocol, and organoids were resuspended in TrypLE at 37°C for 15 min, with vigorous homogenization through a p200 pipette tip every 5 min. After 15 min, the suspension was passed through a 30 μm cell strainer twice and counted under bright-field microscopy with trypan blue staining for viable single cells. For human organoid scRNA-seq, antibody-based cell hashing was performed, with all samples pooled following labelling and three washes in FACS buffer to remove excess antibody. Each sample was manually counted to equally weight in cell pools, and then the pool was split and processed as four identical samples.

We utilized Seq-Well S³ for massively parallel scRNA-seq, for which full methods are published³⁶ and made available on the Shalek Lab website (www.shaleklab.com). Briefly, ~15,000–20,000 cells were loaded onto a functionalized-polydimethylsiloxane (PDMS) array preloaded with ~80,000 uniquely barcoded mRNA capture beads (Chemgenex; MACOSKO-2011-10). After cells had settled into wells, the array was then sealed with a hydroxylated polycarbonate membrane with pore size of 10 nm, facilitating buffer exchange while confining biological molecules within each well. Following membrane-sealing, buffer exchange across the membrane permitted cell lysis, mRNA transcript hybridization to beads and bead removal before proceeding with reverse transcription. The obtained bead-bound complementary DNA (cDNA) product then underwent Exonuclease I treatment (New England Biolabs; M0293M) to remove excess primer before proceeding with second strand synthesis.

Following Exonuclease I treatment, the beads were mixed with 0.1 M NaOH for 5 min at r.t. to denature the mRNA–cDNA hybrid product on the bead. Second strand synthesis was performed with a mastermix consisting of 40 μl 5x maxima RT buffer, 80 μl 30% PEG8000 solution, 20 μl 10 mM dNTPs, 2 μl 1 mM dn-SMART oligo, 5 μl Klenow Exo- and 53 μl DI ultrapure water, with the mastermix being added to the beads and incubated for 1 h at 37°C with end-over-end rotation. After the second strand synthesis, PCR amplification was performed using KAPA HiFi PCR Mix (Kapa Biosystems, KK2602). Specifically, a 40 μl PCR Mastermix consisting of 25 μl KAPA 5X Mastermix, 0.4 μl 100 μM ISPCR oligo and 14.6 μl nuclease-free water was combined with 2,000 beads per reaction. Following PCR amplification, whole transcriptome products were isolated through two rounds of SPRI purification using Ampure Spri beads (Beckman Coulter) at both 0.6X and 0.8X volumetric ratio and quantified using a Qubit. For the antibody hashed human organoid samples, the first SPRI supernatant was retained and subjected to an additional SPRI at 2X final volumetric ratio and quantified using a Qubit. The hashing library then went through a round of step-up PCR to append sequencing handles and indices, followed by a final 1.6X volumetric ratio SPRI before final pooling with the mRNA library (below).

Sequencing libraries were constructed from whole transcriptome product using the Nextera Tagmentation method on a total of 800 pg of pooled cDNA library per sample. Tagmented and amplified sequences were purified through two rounds of SPRI purification (0.6X and 0.8X volumetric ratios) yielding library sizes with an average distribution of 500–750 base pairs in length as determined using the Agilent hsD1000 screen tape system (Agilent Genomics). Murine organoid arrays were sequenced within multi-sample pools on an Illumina NovaSeq through the Broad Institute walk-up sequencing core. Human organoid arrays were sequenced within multi-sample pools on an Illumina NextSeq 550 with a v2.5 high output kit (75 cycle). The read structure was paired end with Read 1 starting from a custom read 1 primer containing 20 bases with a 12 bp cell barcode and 8 bp UMI, and Read 2 being 50 bases containing transcript information. Sequencing read alignment was performed using version 2.1.0 of the Dropseq pipeline previously described⁶⁸. For each sequencing run, raw sequencing reads were converted from bcl files to FASTQs using bcl2fastq based on Nextera N700 indices that corresponded to individual samples. Demultiplexed FASTQs were then aligned to the mm10 (murine) or hg19 (human) genome using STAR and the DropSeq pipeline on a cloud-computing platform maintained by the Broad Institute. Individual reads were tagged with a 12 bp barcode and 8 bp UMI contained in Read 1 of each sequencing fragment. Following alignment, reads were grouped by the 12 bp cell barcodes and subsequently collapsed by the 8 bp UMI for digital gene expression (DGE) matrix extraction and generation. Cell hashing FASTQs were processed with CITE-seq-Count (v1.4.2, <https://zenodo.org/record/2590196>) to obtain UMI-collapsed hashing DGE matrices corresponding to the 6 antibody tags.

Murine scRNA-seq analysis. Before analysis, DGE matrices were pre-processed to remove cellular barcodes with <500 unique genes, >35% of UMIs corresponding to mitochondrial genes, low outliers in standardized house-keeping gene expression⁶⁹, >30,000 UMIs and cellular doublets identified through manual inspection and use of the DoubletFinder algorithm⁷⁰. These pre-processed DGEs are deposited as GEO GSE148524 and are available with interactive visualization tools, metadata and digital gene expression matrices at the Broad Institute's Single-Cell Portal (<https://singlecell.broadinstitute.org>) as study SCP1547.

After quality and doublet correction, we performed integrated analysis on a combined dataset of 19,877 cells, with quality metrics for gene number, captured UMIs and percent mitochondrial genes reported in Extended Data Fig. 2. To better control for potential batch effects that may arise in sample handling and library preparation, dimensional reduction and clustering were performed following

normalization with regularized negative binomial regression as implemented in Seurat V3 via SCTransform⁷¹. We performed variable gene identification and dimensionality reduction utilizing the first 9 principal components based on the elbow method to identify 8 clusters using Louvain clustering (Resolution, 0.45). Following UMAP visualization, we used log-normalized RNA expression for all differential gene expression tests, gene-set enrichment analyses and gene module scoring. Of the 8 original clusters, a single cluster had mixed marker expression corresponding to the secretory goblet and Paneth lineages. Accordingly, we subsetted this cluster and performed variable gene selection and dimensional reduction (14 principal components), and identified 2 previously unreported clusters corresponding to goblet and early secretory cells by Louvain clustering (Resolution, 0.3), which were annotated accordingly in the full dataset. We identified genes enriched across clusters using the Wilcoxon rank sum test, with genes expressed in at least 20% of cells and with a minimum log fold change of 0.5 to identify generic cell types, and corroborated these cell type identities relative to gene signatures coming from an established murine small intestinal scRNA-seq atlas³⁷. Gene modules were scored within each cell on the basis of enrichment in gene set expression relative to randomly selected genes of comparable expression levels in each cell⁶⁹, via the AddModuleScore function within Seurat v3. In addition to cell-type module scoring from ref. ³⁷, we incorporated gene sets for ISC sub-typing from ref. ⁶, in addition to gene sets representing ISC activity¹⁶ and genes known to contain NES from the ValidNESs database³⁹.

To quantify enrichments in cell populations between treatment and control within the murine dataset, we utilized Fisher's exact test for each cell type relative to all others at each timepoint. We only considered populations for testing when that cell type accounted for at least 0.5% of cells in both KPT-330 and control samples. We present the relative enrichment or depletion of a cell population with KPT-330 treatment over time as the odds ratio with a corresponding 95% confidence interval, and false discovery rate (FDR)-adjusted *P* values with significance denoted as *'s in corresponding figure legends.

To interrogate differences in signalling pathway activity between cell types and treatment conditions in the organoid differentiation experiment, we employed the PROGENy package³⁸ to infer pathway activity across the package's 14 supported pathways. Pathway activity was inferred on a single-cell basis without permutation and the top 300 genes were used to generate the model matrix, which was appended as a Seurat object assay in accordance with the PROGENy tutorial for scRNA-seq (<https://saezlab.github.io/progeny/articles/ProgenySingleCell.html>). Pathway activity for the untreated populations is presented as scaled means of pathway activity for each cell type, while Cohen's *d* was calculated between the single-cell distributions of KPT-330-treated and untreated cells.

To interrogate potential differences in upstream TF activity between cell types and treatment conditions of the organoid differentiation experiment, we employed the DoRothEA package³⁸ to infer upstream TF activity in each single cell. Upstream TF activity was inferred on a single-cell basis with the default murine regulon and a minimum of 10 targets per regulon, which was appended as a Seurat object assay in accordance with the DoRothEA tutorial for scRNA-seq (https://saezlab.github.io/dorothea/articles/single_cell_vignette.html). We performed dimensionality reduction on the full DoRothEA assay utilizing the first 7 principal components based on the elbow method to identify 7 clusters using Louvain clustering (Resolution, 0.45). Following UMAP visualization, we used the DoRothEA assay to perform differential upstream TF expression testing, identifying marker TFs for each cluster. To quantify enrichments in upstream TF clusters by cell type between treatment and control, we utilized Fisher's exact test for each cell type relative to all others for each DoRothEA cluster. We only considered populations for testing when that cell type had at least 10 cells originating from both KPT-330 and control samples within that DoRothEA cluster. We present the relative enrichment or depletion of a cell population with KPT-330 treatment in each DoRothEA cluster as the odds ratio with a corresponding 95% confidence interval, and FDR-adjusted *P* values with significance denoted as *'s in corresponding figure legends.

GSEA was performed on the full rank-ordered list of differentially expressed genes (without fold change or *P*-value cutoffs) using the piano R package⁷² and the MsigDB hallmark v7 gene sets^{44,45}. Gene sets with at least 25 and no more than 500 matching genes were considered, and only gene sets with an FDR-corrected *P* < 0.05 were retained.

Human scRNA-seq analysis. Before analysis, DGE matrices were pre-processed to remove cellular barcodes with <500 unique genes, >35% of UMIs corresponding to mitochondrial genes, low outliers in standardized house-keeping gene expression⁶⁹ and >30,000 UMIs. Antibody hashed arrays were demultiplexed with doublets and negative-staining cells removed following default settings of the Seurat function HTODemux. These pre-processed DGEs are deposited in the Broad Institute Single Cell Portal (<https://singlecell.broadinstitute.org>) as study SCP1318.

We performed integrated analysis on a combined dataset of 2,484 cells, with quality metrics for gene number, captured UMIs and percent mitochondrial genes reported in Extended Data Fig. 6. Dimensional reduction and clustering were performed following normalization in Seurat V3 via SCTransform⁷¹. We performed variable gene identification and dimensionality reduction utilizing the first 18 principal components based on the elbow method to identify 7 clusters using Louvain clustering (Resolution, 0.5). Following UMAP visualization, we

used log-normalized RNA expression for all differential gene expression tests, gene-set enrichment analyses and gene module scoring. Of the 7 original clusters, a single cluster had mixed marker expression corresponding to the secretory goblet and enteroendocrine lineages. Accordingly, we subsetted this cluster and performed variable gene selection and dimensional reduction (8 principal components), and identified 2 previously unreported clusters corresponding to goblet and enteroendocrine cells by Louvain clustering (Resolution, 0.3), which were annotated accordingly in the full dataset. We identified genes enriched across clusters using the Wilcoxon rank sum test, with genes expressed in at least 10% of cells and with a minimum log fold change of 0.25 to identify cell types, and corroborated these cell type identities relative to known gene markers. Gene modules were scored within each cell on the basis of enrichment in gene set expression relative to randomly selected genes of comparable expression levels in each cell⁶⁹, via the AddModuleScore function within Seurat v3 (for genes known to contain NES, from the ValidNESs database³⁹).

To quantify enrichments in cell populations between treatment and control within the human dataset, we utilized Fisher's exact test for each cell type relative to all others by donor. We only considered populations for testing when that cell type had at least 1 cell in both KPT-330 and control samples. We present the relative enrichment or depletion of a cell population with KPT-330 treatment over time as the odds ratio with a corresponding 95% confidence interval, and FDR-adjusted *P* values with significance denoted as *'s in corresponding figure legends.

To interrogate differences in signalling pathway activity between cell types and treatment conditions in the human organoid experiment, we employed the PROGENy package³⁸ to infer pathway activity across the package's 14 supported pathways. Pathway activity was inferred on a single-cell basis without permutation and the top 300 genes were used to generate the model matrix, which was appended as a Seurat object assay in accordance with the PROGENy tutorial for scRNA-seq (<https://saezlab.github.io/progeny/articles/ProgenySingleCell.html>). Pathway activity for the untreated populations is presented as scaled means of pathway activity for each cell type.

Reporting Summary. Further information on research design is available in the Nature Research Reporting Summary linked to this article.

Data availability

Source data for the figures are provided with this paper. The murine scRNA-seq data are available from the NCBI Gene Expression Omnibus under accession number GSE148524. Interactive visualization tools, metadata and digital gene-expression matrices can be found via the Broad Institute's Single-Cell Portal (<https://singlecell.broadinstitute.org>; studies SCP1547 and SCP1318). To protect the genetic information of donors, FASTQ data for the human intestinal organoids are available on request from A.K.S., provided that a data-use agreement can be signed. The ValidNESS database was accessed via <http://validness.ym.edu.tw>. Source data are provided with this paper.

Code availability

The analysis scripts for screening and scRNA-seq are available at https://github.com/ShalekLab/Mead_et_al_NatBME_2021.

Received: 5 August 2020; Accepted: 3 February 2022;
Published online: 21 March 2022

References

- Ordovas-Montanes, J. et al. Allergic inflammatory memory in human respiratory epithelial progenitor cells. *Nature* **560**, 649–654 (2018).
- Naik, S. et al. Inflammatory memory sensitizes skin epithelial stem cells to tissue damage. *Nature* **550**, 475–480 (2017).
- Smillie, C. S. et al. Intra- and inter-cellular rewiring of the human colon during ulcerative colitis. *Cell* **178**, 714–730.e22 (2019).
- Roulis, M. et al. Paracrine orchestration of intestinal tumorigenesis by a mesenchymal niche. *Nature* <https://doi.org/10.1038/s41586-020-2166-3> (2020).
- Beyaz, S. et al. High-fat diet enhances stemness and tumorigenicity of intestinal progenitors. *Nature* **531**, 53–58 (2016).
- Biton, M. et al. T helper cell cytokines modulate intestinal stem cell renewal and differentiation. *Cell* <https://doi.org/10.1016/j.cell.2018.10.008> (2018).
- von Moltke, J., Ji, M., Liang, H. & Locksley, R. M. Tuft-cell-derived IL-25 regulates an intestinal ILC2–epithelial response circuit. *Nature* **529**, 221–225 (2016).
- Horvath, P. et al. Screening out irrelevant cell-based models of disease. *Nat. Rev. Drug Discov.* **15**, 751–769 (2016).
- Sato, T. et al. Single Lgr5 stem cells build crypt-villus structures in vitro without a mesenchymal niche. *Nature* **459**, 262–265 (2009).
- Yin, X. et al. Niche-independent high-purity cultures of Lgr5+ intestinal stem cells and their progeny. *Nat. Methods* **11**, 106–112 (2014).
- Mead, B. E. et al. Harnessing single-cell genomics to improve the physiological fidelity of organoid-derived cell types. *BMC Biol.* **16**, 62 (2018).

12. Serra, D. et al. Self-organization and symmetry breaking in intestinal organoid development. *Nature* <https://doi.org/10.1038/s41586-019-1146-y> (2019).
13. Lukonin, I. et al. Phenotypic landscape of intestinal organoid regeneration. *Nature* **586**, 275–280 (2020).
14. Czerniecki, S. M. et al. High-throughput screening enhances kidney organoid differentiation from human pluripotent stem cells and enables automated multidimensional phenotyping. *Cell Stem Cell* **22**, 929–940.e4 (2018).
15. Sachs, N. et al. A living biobank of breast cancer organoids captures disease heterogeneity. *Cell* **172**, 373–386.e10 (2018).
16. van de Wetering, M. et al. Prospective derivation of a living organoid biobank of colorectal cancer patients. *Cell* **161**, 933–945 (2015).
17. Ringel, T. et al. Genome-scale CRISPR screening in human intestinal organoids identifies drivers of TGF- β resistance. *Cell Stem Cell* **26**, 431–440.e8 (2020).
18. Mead, B. E. & Karp, J. M. All models are wrong, but some organoids may be useful. *Genome Biol.* **20**, 66 (2019).
19. Danahay, H. et al. Notch2 is required for inflammatory cytokine-driven goblet cell metaplasia in the lung. *Cell Rep.* **10**, 239–252 (2015).
20. McGuckin, M. A., Eri, R., Simms, L. A., Florin, T. H. J. & Radford-Smith, G. Intestinal barrier dysfunction in inflammatory bowel diseases. *Inflamm. Bowel Dis.* **15**, 100–113 (2009).
21. Liu, T.-C. et al. Paneth cell defects in Crohn's disease patients promote dysbiosis. *JCI Insight* **1**, e86907 (2016).
22. Gassler, N. Paneth cells in intestinal physiology and pathophysiology. *World J. Gastrointest. Pathophysiol.* **8**, 150–160 (2017).
23. McElroy, S. J., Underwood, M. A. & Sherman, M. P. Paneth cells and necrotizing enterocolitis: a novel hypothesis for disease pathogenesis. *Neonatology* **103**, 10–20 (2013).
24. Liu, T. C. et al. A novel histological index for evaluation of environmental enteric dysfunction identifies geographic-specific features of enteropathy among children with suboptimal growth. *PLoS Negl. Trop. Dis.* **14**, e0007975 (2020).
25. Eriguchi, Y. et al. Graft-versus-host disease disrupts intestinal microbial ecology by inhibiting Paneth cell production of α -defensins. *Blood* **120**, 223–231 (2012).
26. Hayase, E. et al. R-Spondin1 expands Paneth cells and prevents dysbiosis induced by graft-versus-host disease. *J. Exp. Med.* **214**, 3507–3518 (2017).
27. Han, T. et al. R-Spondin chromosome rearrangements drive Wnt-dependent tumour initiation and maintenance in the intestine. *Nat. Commun.* **8**, 15945 (2017).
28. Fre, S. et al. Notch signals control the fate of immature progenitor cells in the intestine. *Nature* **435**, 964–968 (2005).
29. Langhans, S. A. Three-dimensional in vitro cell culture models in drug discovery and drug repositioning. *Front. Pharmacol.* **9**, <https://doi.org/10.3389/fphar.2018.00006> (2018).
30. Gunasekara, D. B. et al. Development of arrayed colonic organoids for screening of secretagogues associated with enterotoxins. *Anal. Chem.* **90**, 1941–1950 (2018).
31. Zhang, X. D. in *Optimal High-Throughput Screening* 83–108 (Cambridge Univ. Press, 2011). <https://doi.org/10.1017/CBO9780511973888.007>
32. Sun, Q. et al. Inhibiting cancer cell hallmark features through nuclear export inhibition. *Signal Transduct. Target. Ther.* **1**, 34–36 (2016).
33. Wang, A. Y. & Liu, H. The past, present, and future of CRM1/XPO1 inhibitors. *Stem Cell Investig.* **6**, <https://doi.org/10.21037/sci.2019.02.03> (2019).
34. Sendino, M., Omaetxebarria, M. J. & Rodriguez, J. A. Hitting a moving target: inhibition of the nuclear export receptor XPO1/CRM1 as a therapeutic approach in cancer. *Cancer Drug Resist.* <https://doi.org/10.20517/cdr.2018.09> (2018).
35. Forbes, D. J., Travesa, A., Nord, M. S. & Bernis, C. Nuclear transport factors: global regulation of mitosis. *Curr. Opin. Cell Biol.* **35**, 78–90 (2015).
36. Hughes, T.K., et al. Second-Strand Synthesis-Based Massively Parallel scRNA-Seq Reveals Cellular States and Molecular Features of Human Inflammatory Skin Pathologies. *Immunity* **53**, <https://doi.org/10.1016/j.immuni.2020.09.015> (2020).
37. Haber, A. L. et al. A single-cell survey of the small intestinal epithelium. *Nature* <https://doi.org/10.1038/nature24489> (2017).
38. Holland, C. H. et al. Robustness and applicability of transcription factor and pathway analysis tools on single-cell RNA-seq data. *Genome Biol.* **21**, <https://doi.org/10.1186/s13059-020-1949-z> (2020).
39. Fu, S. C., Huang, H. C., Horton, P. & Juan, H. F. ValidNESs: a database of validated leucine-rich nuclear export signals. *Nucleic Acids Res.* **41**, 338–343 (2013).
40. Draheim, K. M. et al. ARRDC3 suppresses breast cancer progression by negatively regulating integrin B4. *Oncogene* **29**, 5032–5047 (2010).
41. Cheng, C.-W. et al. Ketone body signaling mediates intestinal stem cell homeostasis and adaptation to diet. *Cell* **178**, 1115–1131.e15 (2019).
42. Zhou, J., Edgar, B. A. & Boutros, M. ATF3 acts as a rheostat to control JNK signalling during intestinal regeneration. *Nat. Commun.* **8**, <https://doi.org/10.1038/ncomms14289> (2017).
43. Jadhav, K. & Zhang, Y. Activating transcription factor 3 in immune response and metabolic regulation. *Liver Res.* **1**, 96–102 (2017).
44. Subramanian, A. et al. Gene set enrichment analysis: a knowledge-based approach for interpreting genome-wide expression profiles. *Proc. Natl Acad. Sci. USA* **102**, 15545–15550 (2005).
45. Liberzon, A. et al. The molecular signatures database hallmark gene set collection. *Cell Syst.* **1**, 417–425 (2015).
46. Basak, O. et al. Induced quiescence of Igr5+ stem cells in intestinal organoids enables differentiation of hormone-producing enteroendocrine cells. *Cell Stem Cell* **20**, 177–190.e4 (2017).
47. Fujii, M. et al. Human intestinal organoids maintain self-renewal capacity and cellular diversity in niche-inspired culture condition. *Cell Stem Cell* **23**, 787–793.e6 (2018).
48. Miyoshi, H. et al. Prostaglandin E2 promotes intestinal repair through an adaptive cellular response of the epithelium. *EMBO J.* **36**, 5–24 (2017).
49. Goldenring, J. R. Pyloric metaplasia, pseudopyloric metaplasia, ulcer-associated cell lineage and spasmolytic polypeptide-expressing metaplasia: reparative lineages in the gastrointestinal mucosa. *J. Pathol.* **245**, 132–137 (2018).
50. Grasberger, H. et al. Increased expression of DUOX2 is an epithelial response to mucosal dysbiosis required for immune homeostasis in mouse intestine. *Gastroenterology* **149**, 1849–1859 (2015).
51. Ireland, H., Houghton, C., Howard, L. & Winton, D. J. Cellular inheritance of a Cre-activated reporter gene to determine paneth cell longevity in the murine small intestine. *Dev. Dyn.* **233**, 1332–1336 (2005).
52. Azmi, A. S. et al. Selective inhibitors of nuclear export block pancreatic cancer cell proliferation and reduce tumor growth in mice. *Gastroenterology* **144**, 447–456 (2013).
53. Hing, Z. A. et al. Next-generation XPO1 inhibitor shows improved efficacy and in vivo tolerability in hematological malignancies. *Leukemia* **30**, 2364–2372 (2016).
54. Zheng, Y. et al. KPT-330 inhibitor of XPO1-mediated nuclear export has anti-proliferative activity in hepatocellular carcinoma. *Cancer Chemother. Pharmacol.* **74**, 487–495 (2014).
55. Arango, N. P. et al. Selinexor (KPT-330) demonstrates anti-tumor efficacy in preclinical models of triple-negative breast cancer. *Breast Cancer Res.* **19**, 93 (2017).
56. Tyler, P. M. et al. Clinical dosing regimen of selinexor maintains normal immune homeostasis and t-cell effector function in mice: implications for combination with immunotherapy. *Mol. Cancer Ther.* **16**, 428–439 (2017).
57. Abraham, C. & Cho, J. H. Inflammatory bowel disease. *N. Engl. J. Med.* **361**, 2066–2078 (2009).
58. Yang, H. W., Chung, M., Kudo, T. & Meyer, T. Competing memories of mitogen and p53 signalling control cell-cycle entry. *Nature* **549**, 404–408 (2017).
59. Ayyaz, A. et al. Single-cell transcriptomes of the regenerating intestine reveal a revival stem cell. *Nature* **569**, 121–125 (2019).
60. Yousefi, M., Li, L. & Lengner, C. J. Hierarchy and plasticity in the intestinal stem cell compartment. *Trends Cell Biol.* **27**, 753–764 (2017).
61. De Jong, P. R. et al. ERK5 signalling rescues intestinal epithelial turnover and tumour cell proliferation upon ERK1/2 abrogation. *Nat. Commun.* **7**, <https://doi.org/10.1038/ncomms11551> (2016).
62. Heuberger, J. et al. Shp2/MAPK signaling controls goblet/paneth cell fate decisions in the intestine. *Proc. Natl Acad. Sci. USA* **111**, 3472–3477 (2014).
63. Glal, D. et al. ATF3 sustains IL-22-induced STAT3 phosphorylation to maintain mucosal immunity through inhibiting phosphatases. *Front. Immunol.* **9**, <https://doi.org/10.3389/fimmu.2018.02522> (2018).
64. Negggers, J. E. et al. Identifying drug-target selectivity of small-molecule CRM1/XPO1 inhibitors by CRISPR/Cas9 genome editing. *Chem. Biol.* **22**, 107–116 (2015).
65. Miyoshi, H. & Stappenbeck, T. S. In vitro expansion and genetic modification of gastrointestinal stem cells in spheroid culture. *Nat. Protoc.* **8**, 2471–2482 (2013).
66. Mpindi, J. P. et al. Impact of normalization methods on high-throughput screening data with high hit rates and drug testing with dose-response data. *Bioinformatics* **31**, 3815–3821 (2015).
67. Zhang, X. D. Illustration of SSMD, z score, SSMD*, z* score, and t statistic for hit selection in RNAi high-throughput screens. *J. Biomol. Screen.* **16**, 775–785 (2011).
68. Macosko, E. Z. et al. Highly parallel genome-wide expression profiling of individual cells using nanoliter droplets. *Cell* **161**, 1202–1214 (2015).
69. Tirosch, I. et al. Dissecting the multicellular ecosystem of metastatic melanoma by single-cell RNA-seq. *Science* **352**, 189–196 (2016).
70. McGinnis, C. S., Murrow, L. M. & Gartner, Z. J. DoubletFinder: doublet detection in single-cell rna sequencing data using artificial nearest neighbors. *Cell Syst.* **8**, 329–337.e4 (2019).
71. Hafemeister, C. & Satija, R. Normalization and variance stabilization of single-cell RNA-seq data using regularized negative binomial regression. *Genome Biol.* **20**, 296 (2019).

72. Våremo, L., Nielsen, J. & Nookaew, I. Enriching the gene set analysis of genome-wide data by incorporating directionality of gene expression and combining statistical hypotheses and methods. *Nucleic Acids Res.* **41**, 4378–4391 (2013).

Acknowledgements

This work was supported in part by Koch Institute Support (core) Grant P30-CA14051 from the National Cancer Institute. We thank S. Nguyen for advice on flow cytometry, and the Koch Institute Swanson Biotechnology Center for technical support, specifically J. Cheah and C. Soule with the High-Throughput Science facility, the Flow Cytometry facility and the Histology facility; the Broad Institute Walk-Up Sequencing core for providing Illumina NovaSeq services; the MIT Stem Cell Initiative through Fondation MIT; and the Harvard Digestive Disease Center and NIH grant P30DK034854 for the provision of reagents. B.E.M. was supported by the National Science Foundation graduate research fellowship programme and the Massachusetts Institute of Technology–GlaxoSmithKline (MIT–GSK) Gertrude B. Elion Postdoctoral fellowship. K.H. received fellowships from The Japanese Biochemical Society (The Osamu Hayaishi Memorial Scholarship for Study Abroad), the Mochida Memorial Foundation for Medical and Pharmaceutical Research, and The Uehara Memorial Foundation. J.O.-M. is a New York Stem Cell Foundation – Robertson Investigator. J.O.M. was supported by the Richard and Susan Smith Family Foundation, the HHMI Damon Runyon Cancer Research Foundation Fellowship (DRG-2274-16), the AGA Research Foundation's AGA-Takeda Pharmaceuticals Research Scholar Award in IBD – AGA2020-13-01, the HDDC Pilot and Feasibility P30DK034854, the Food Allergy Science Initiative, and The New York Stem Cell Foundation. R.L. was supported by the NIH (DE013023). R.S.B. was supported by the NIH (DK088199). A.K.S. was supported by the Beckman Young Investigator Program, the Pew-Stewart Scholars Program for Cancer Research, a Sloan Fellowship in Chemistry, the Bill and Melinda Gates Foundation (OPP1202327/INV-006897), and the NIH (1DP2GM119419, 1U54CA217377). J.M.K. was supported by the Kenneth Rainin Foundation Innovator and Breakthrough awards, the Crohn's and Colitis Foundation (#624458), and the NIH (HL095722). Ö.H.Y. was supported by R01CA211184, R01CA034992, the Pew-Stewart Trust scholar award, the Kathy and Curt Marble Cancer Research Award, and a Bridge grant; A.K.S. and Ö.H.Y. received support from the MIT Stem Cell Initiative through Fondation MIT.

Author contributions

B.E.M., K.H., A.K.S. and J.M.K. conceptualized the study; B.E.M., L.L., D.S., K.H., J.D.M., J.D., R.S.B., N.G., S.I. and O.H.Y. developed the methodology; B.E.M. and D.S. developed the software; A.K.S., J.M.K., R.L., R.S.B. and O.H.Y. provided resources; B.E.M., K.H., L.L., D.S., R.L., J.O.-M., A.K.S. and J.M.K. wrote the original draft; B.E.M., K.H., M.V.,

J.D.M., R.L., J.O.-M., A.K.S., J.M.K., N.G., S.I., O.H.Y. and C.K. wrote and edited revised drafts; B.E.M., K.H., D.S., J.O.-M., A.K.S., J.M.K. and S.I. performed visualization tasks; A.K.S., J.M.K., R.L., J.O.-M. and O.H.Y. supervised the study; B.E.M., K.H., J.O.-M., R.S.B., R.L., A.K.S., J.M.K. and O.H.Y. acquired funding.

Competing interests

J.M.K. and R.L. hold equity in Frequency Therapeutics, a company that has an option to license IP generated by J.M.K. and R.L. and that may benefit financially if the IP is licensed and further validated. The interests of J.M.K. and R.L. were reviewed and are subject to a management plan overseen by their institutions in accordance with their conflict-of-interest policies. J.O.-M. reports compensation for consulting services with Cellarity and Hovione. A.K.S. reports compensation for consulting and/or SAB membership from Merck, Honeycomb Biotechnologies, Cellarity, Repertoire Immune Medicines, Third Rock Ventures, Ochre Bio, FL82, Relation Therapeutics Limited, and Dahlia Biosciences. The other authors declare no competing interests.

Additional information

Extended data is available for this paper at <https://doi.org/10.1038/s41551-022-00863-9>.

Supplementary information The online version contains supplementary material available at <https://doi.org/10.1038/s41551-022-00863-9>.

Correspondence and requests for materials should be addressed to Jeffrey M. Karp or Alex K. Shalek.

Peer review information *Nature Biomedical Engineering* thanks Matthias Lutolf and the other, anonymous, reviewer(s) for their contribution to the peer review of this work.

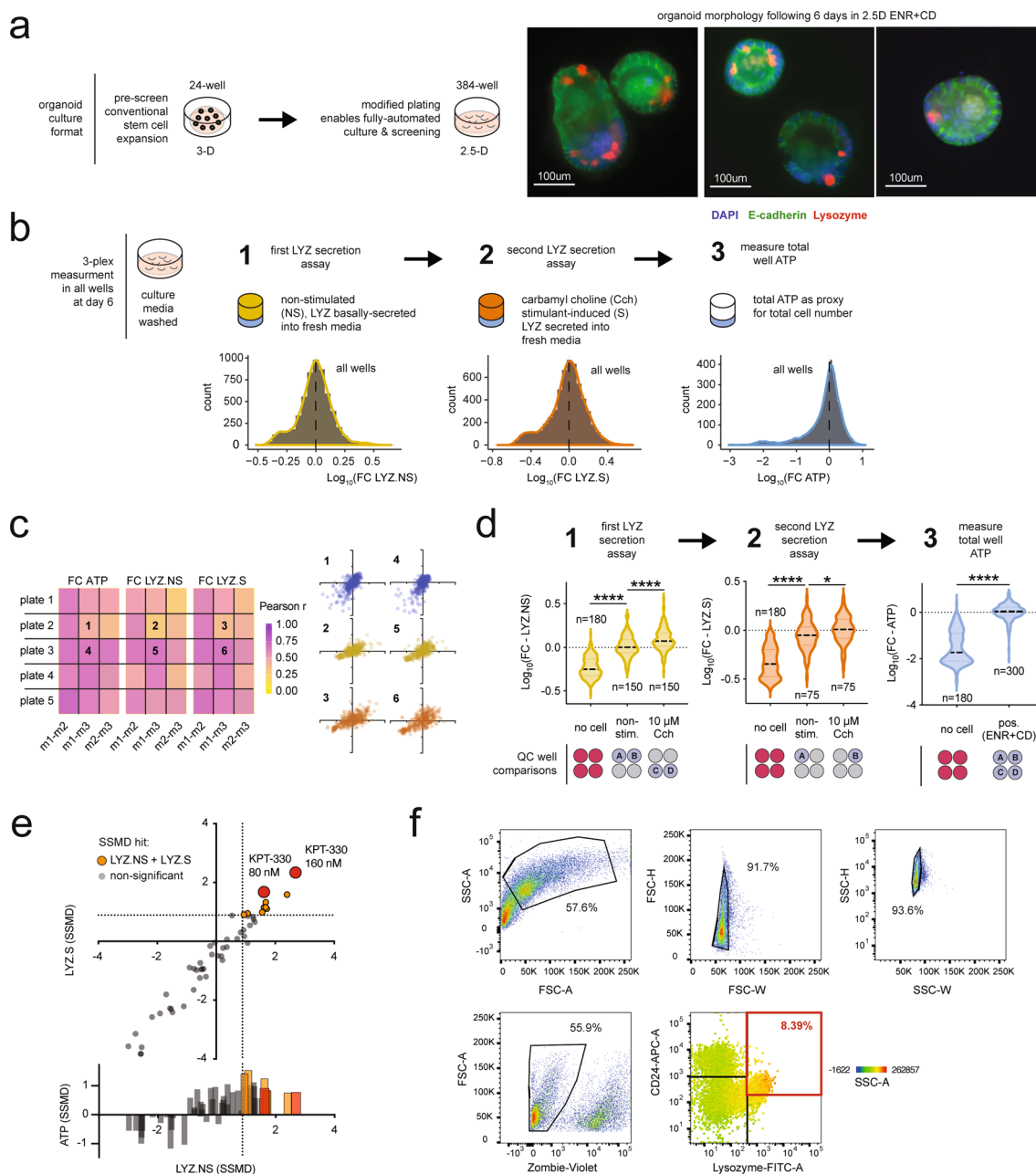
Reprints and permissions information is available at www.nature.com/reprints.

Publisher's note Springer Nature remains neutral with regard to jurisdictional claims in published maps and institutional affiliations.

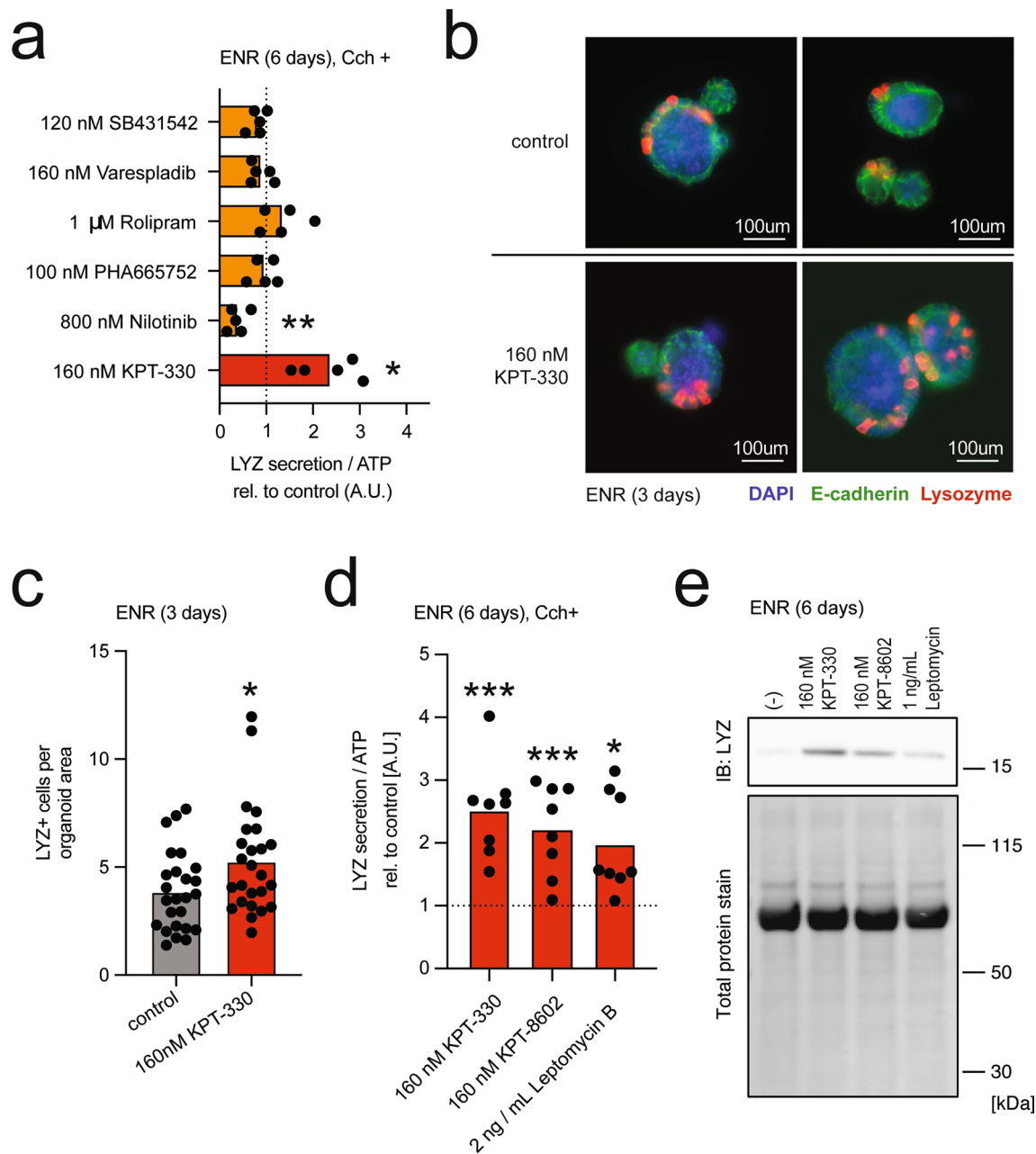


Open Access This article is licensed under a Creative Commons Attribution 4.0 International License, which permits use, sharing, adaptation, distribution and reproduction in any medium or format, as long as you give appropriate credit to the original author(s) and the source, provide a link to the Creative Commons license, and indicate if changes were made. The images or other third party material in this article are included in the article's Creative Commons license, unless indicated otherwise in a credit line to the material. If material is not included in the article's Creative Commons license and your intended use is not permitted by statutory regulation or exceeds the permitted use, you will need to obtain permission directly from the copyright holder. To view a copy of this license, visit <http://creativecommons.org/licenses/by/4.0/>.

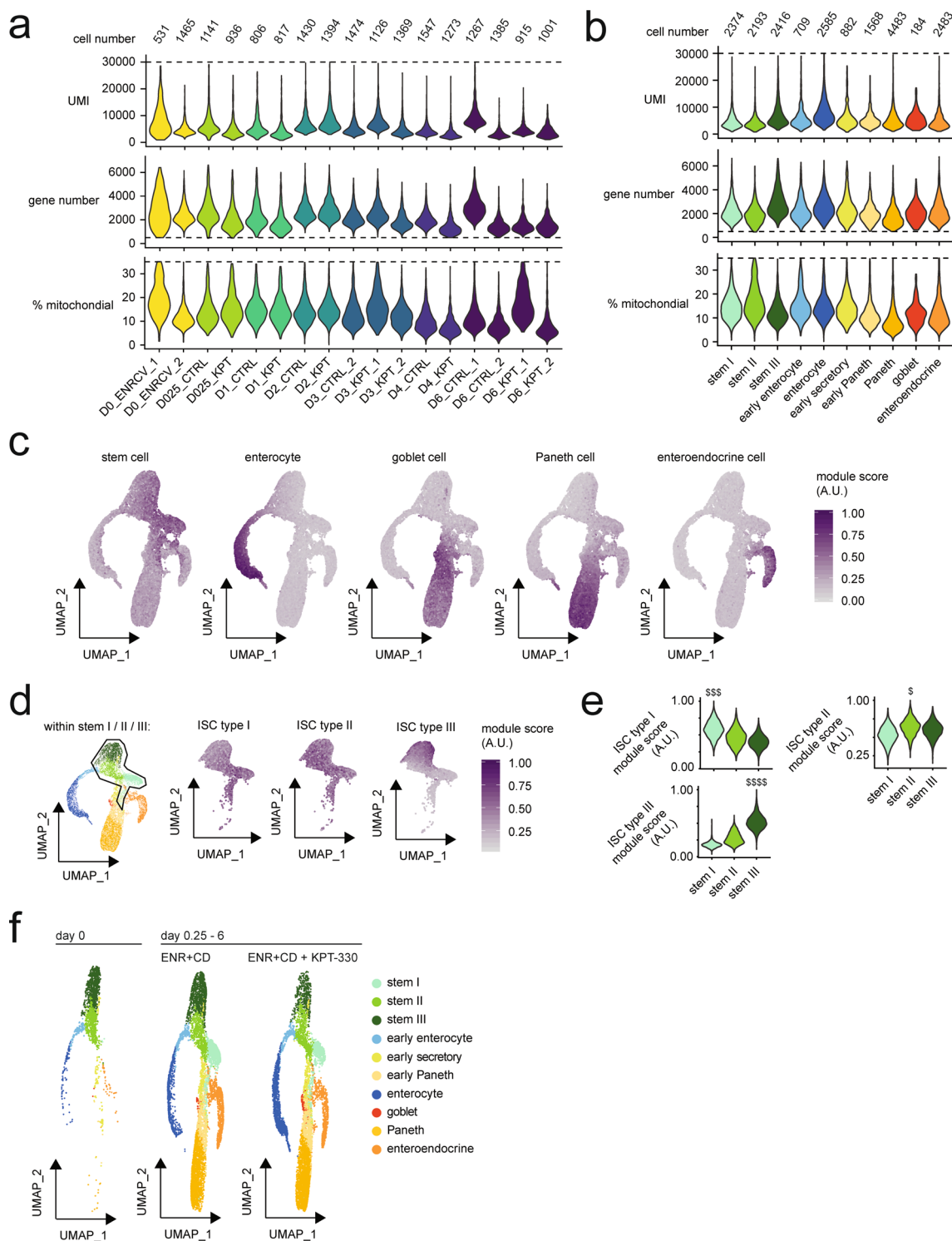
© The Author(s) 2022



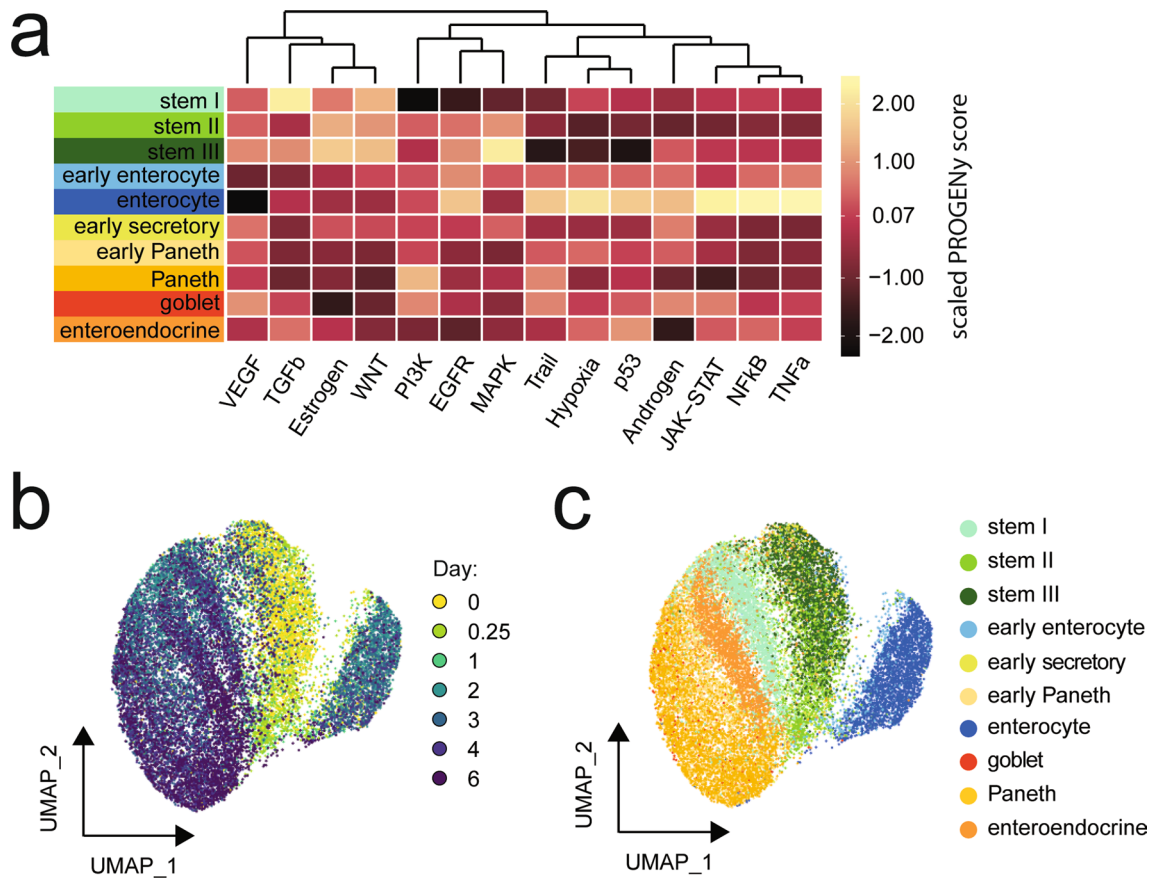
Extended Data Fig. 1 | Characterization of small intestinal organoid screening approach. **a**, Organoids grown in stem-enriched media and transferred to culture in 2.5D system for 6 d (ENR + CD), Paneth cells marked by Lysozyme, representative image of 3 from single experiment shown. **b**, Tri-plex assay order and distributions of all sample data (N = 5676 wells) for each assay (numbered by order of assay) following data transformation and normalization, dotted line indicates median of distribution from which fold change calculations are determined. **c**, Pearson correlation (r) between all sample wells by screen plate and biological replicate (m1, m2, m3), with representative correlation plots shown for assay plates 1 through 6. **d**, ATP, LYZ.NS, LYZ.S assay quality control comparisons across all plates and replicates, functional control wells chosen for comparison based on presence (S) or absence (NS) of Cch-stimulation in first (LYZ.NS) and second (LYZ.S) secretion assays. One-tailed Welch's t test for ATP; **** adj. $p < 0.0001$, one-way ANOVA post-hoc Dunnett's multiple comparison test * adj. $p = 0.0224$, **** adj. $p < 0.0001$. **e**, Replicate strictly standardized mean difference (SSMD) for each assay in secondary validation screen, each point represents the SSMD from 8 well-replicates relative to DMSO control, orange signifies treatments passing cutoffs in both LYZ.NS and LYZ.S assays, red marking most potent compound, KPT-330. **f**, Flow cytometry gating strategy to select viable mature Paneth cells, final gate outlined in red.



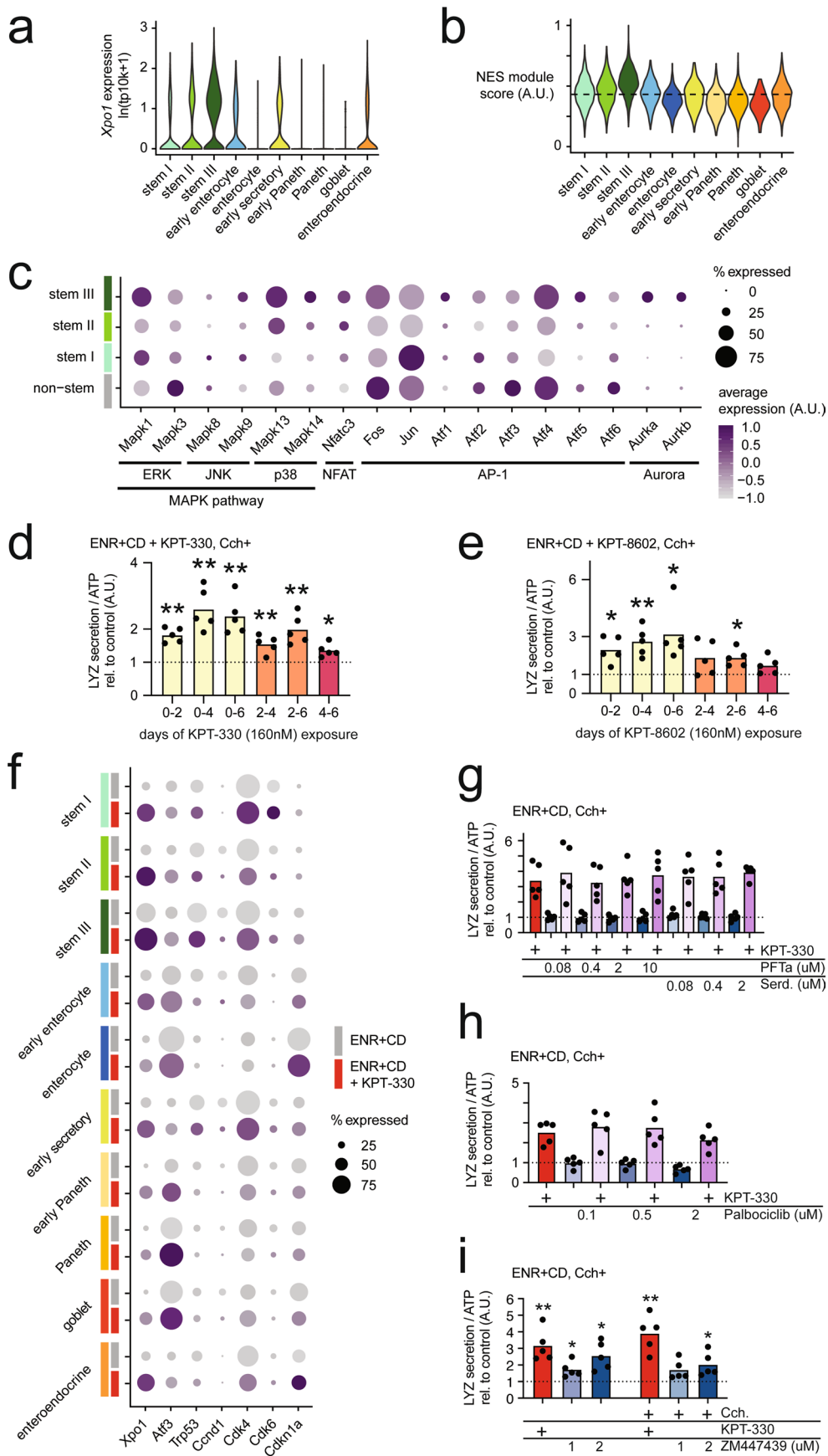
Extended Data Fig. 2 | Profiling small molecule hits from Paneth cell-directed murine organoid screen. **a**, LYZ secretion assay for organoids differentiated in ENR with 6 hit compounds for 6 days. Organoids incubated in fresh basal media with 10 μ M carbachol (Cch) for 3 h on day 6. All data normalized to ATP abundance and standardized to the control in each experiment. Means and individual values are shown (N=5), dotted line represents the control value (1). One sample t-test compared to 1; **p=0.0023, *p=0.0101. **b**, Representative immunofluorescence images of 25 total organoids differentiated in ENR media with 160 nM KPT-330 for 3 days, Paneth cells marked by LYZ. **c**, Quantification of immunofluorescent images for LYZ+ cells per organoid area for organoids differentiated in ENR with 160 nM KPT-330 for 3 days. Means and individual values are shown (N=25 organoids). Unpaired two-tailed t-test; *p=0.0275. **d**, LYZ secretion assay for organoids differentiated in ENR with 160 nM KPT-330, 160 nM KPT-8602 or 2 ng/mL Leptomycin B for 6 days. Organoids incubated in fresh basal media with 10 μ M carbachol (Cch) for 3 h on day 6. All data normalized to ATP abundance and standardized to the control in each experiment. Means and individual values are shown (N=5), dotted line represents the control value (1). One sample t-test compared to 1; ordered left to right, ***p=0.0007, ***p=0.0021, *p=0.0095. **e**, Western blotting of intracellular LYZ in 3D-cultured intestinal organoids, cultured in ENR media for 6 days (N=1).



Extended Data Fig. 3 | Single-cell RNA-seq profiling of murine organoid differentiation with KPT-330-mediated XPO1 inhibition. a, Single-cell RNA-seq quality metrics on a per-sample basis, including final cell number (barcodes) per array, and distributions of unique molecular identifiers per barcode (UMI), unique gene number per barcode, and percent of total UMIs corresponding to mitochondrial genes per barcode. **b**, Single-cell RNA-seq quality metrics on a per-cell type basis, including final cell number (barcodes) per array, and distributions of unique molecular identifiers per barcode (UMI), unique gene number per barcode, and percent of total UMIs corresponding to mitochondrial genes per barcode. **c**, Feature plots over organoid differentiation UMAP representing module scores derived from gene sets enriched in *in vivo* stem cells, enterocytes, goblet cells, Paneth cells, and enteroendocrine cells, each score scaled on a range from 0 to 1. **d**, Feature plots over organoid differentiation UMAP restricted to stem I / II / III populations representing module scores derived from gene sets enriched in *in vivo* type I / II / III intestinal stem cells (ISCs), each score scaled on a range from 0 to 1. **e**, Violin plots for stem I / II / III populations representing module scores derived from gene sets enriched in *in vivo* type I / II / III intestinal stem cells (ISCs), each score scaled on a range from 0 to 1. Effect size measured as Cohen's d , $\$$ $0.5 < d < 0.8$, $\$\$\$$ $1.2 < d < 2$, $\$\$\$\$$ $d > 2$. **f**, Organoid differentiation UMAP labeled by annotated cell type, and split by day 0 (ENR + CV), day 0.25–6 control (ENR + CD), and day 0.25–6 160 nM KPT-330-treated (ENR + CD + KPT-330).

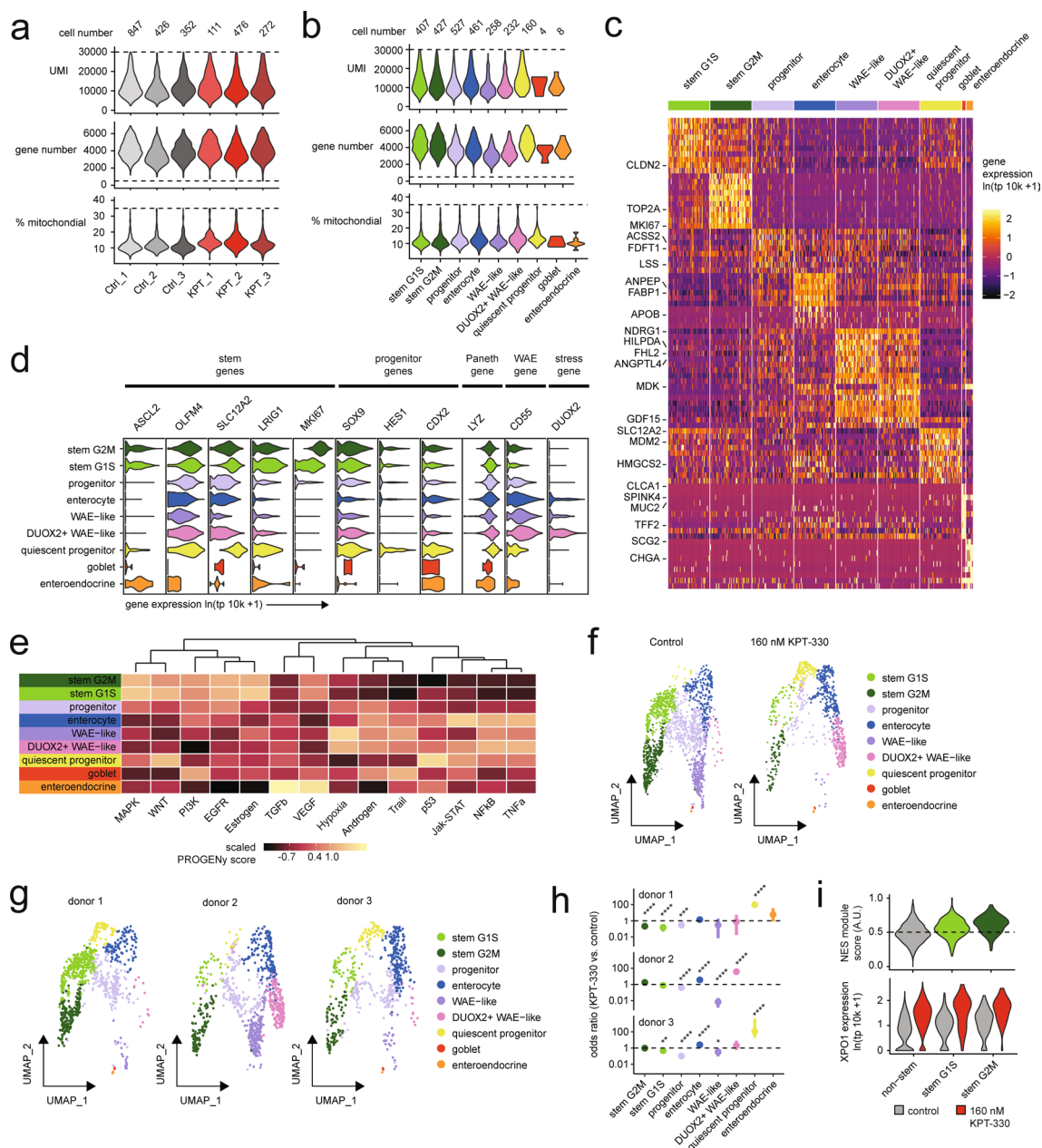


Extended Data Fig. 4 | Pathway and inferred transcription factor landscape of single-cell RNA-seq data from murine organoid differentiation. a, Heatmap of predicted pathway signaling for non-KPT-330-treated cells using PROGENy scores calculated over single-cell RNA-seq data for each cell type. **b,** Organoid single-cell RNA-seq UMAP based on upstream transcription factor (TF) prediction (DoRothEA) of all samples labeled by differentiation timepoint. **c,** Organoid single-cell RNA-seq UMAP based on upstream transcription factor (TF) prediction (DoRothEA) of all samples labeled by annotated cell type.

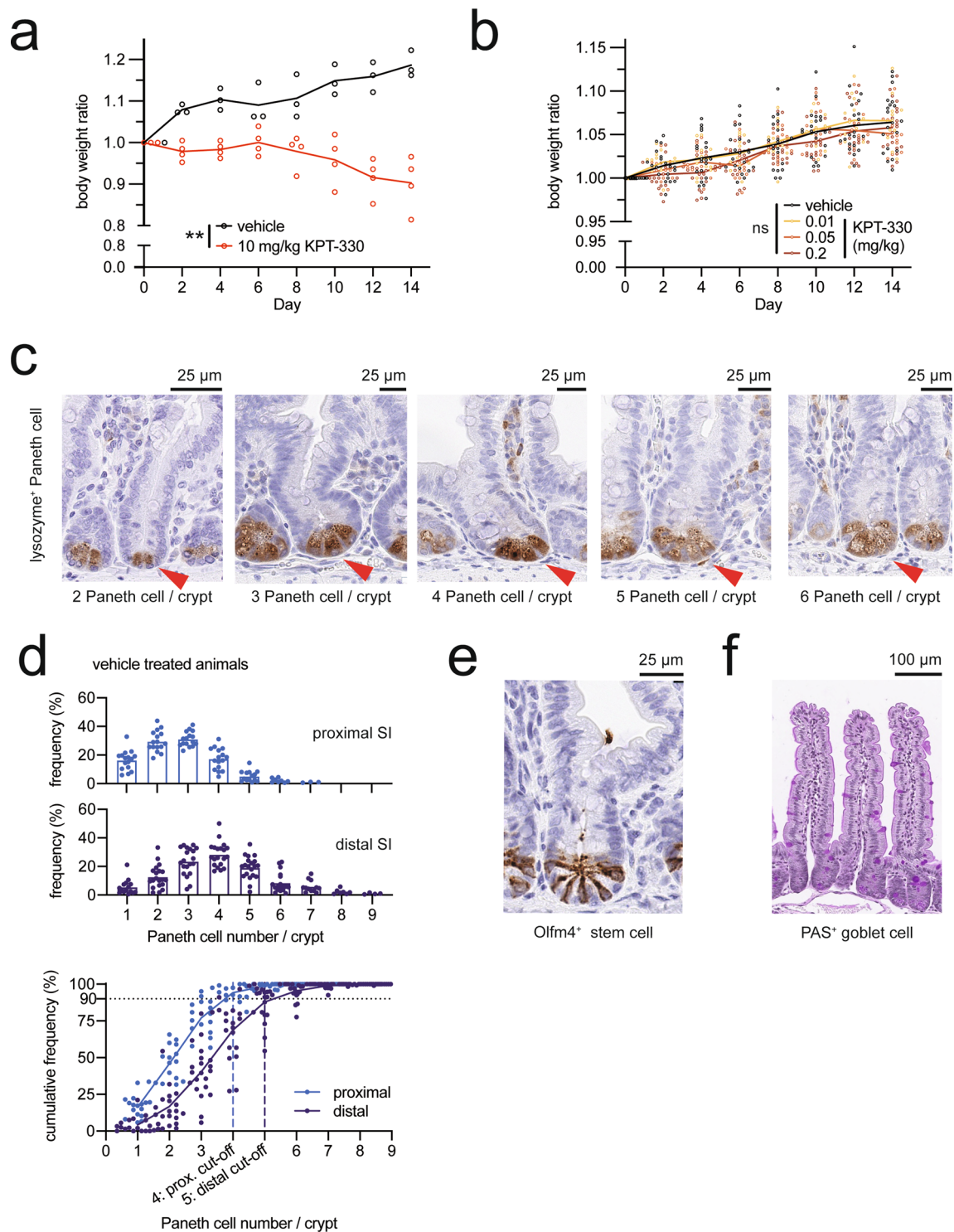


Extended Data Fig. 5 | See next page for caption.

Extended Data Fig. 5 | Signaling pathway analysis of murine organoids with KPT-330-mediated XPO1 inhibition. **a**, Single-cell RNA-seq log normalized (transcripts per 10,000 - tp10k) expression of *Xpo1* in control cells by cell type annotations. **b**, Violin plots of nuclear export signal (NES) containing gene module score in control cells by cell type annotations, scaled from 0 to 1. **c**, Single-cell RNA-seq log normalized expression of genes involved in MAPK, NFAT, AP-1, and Aurora kinase signaling in control cells by non-stem, and stem I / II / III annotations. **d**, LYZ secretion assay for organoids treated with KPT-330 (**d**) or KPT-8602 (**e**) for 6 days culture in ENR + CD media. Organoids were incubated in fresh basal media with 10 μ M carbachol (Cch) for 3 h on day 6. Data normalized to ATP and standardized to the control in each experiment. Means and individual values are shown (N=5), dotted line represents the control value (1). One sample two-tailed t-test compared to 1; significant p values for (**d**) ordered left to right, **p=0.0011, **p=0.0049, **p=0.0053, **p=0.0098, **p=0.0077, *p=0.0156, for (**e**) ordered left to right, *p=0.0132, **p=0.0071, *p=0.0295, *p=0.0124. **f**, Single-cell RNA-seq log normalized expression of genes regulated by XPO1 signaling between KPT-330-treated and control cells by cell-type annotations. Color scale is relative to control, purple-to-grey increasing relative-expression. LYZ secretion assay for organoids treated with p53 modulators, inhibitor Pifithrin- α (PFT α) and activator Serdemetan (Serd.) (**g**), CDK4/6 inhibitor Palbociclib (**h**), Aurora kinase inhibitor ZM447439 (**i**), over 6-day culture in ENR + CD media with or without 160 nM KPT-330. Organoids were incubated in fresh basal media with 10 μ M carbachol (Cch) for 3 h on day 6. Data normalized to ATP and standardized to control in each experiment. Means and individual values are shown (N=5), and the dotted line represents the control value (1). One sample two-sided t-test compared to 1; significant p-values for (**i**) ordered left to right, **p=0.0073, *p=0.0259, *p=0.0151, **p=0.0040, *p=0.0331.



Extended Data Fig. 6 | Single-cell RNA-seq analysis for human organoids. **a**, Human organoid single-cell RNA-seq quality metrics on a per-sample basis, including final cell number (barcodes) per array, and distributions of unique molecular identifiers per barcode (UMI), unique gene number per barcode, and percent of total UMIs corresponding to mitochondrial genes per barcode. **b**, Human organoid single-cell RNA-seq quality metrics on a per-cell type basis, including final cell number (barcodes) per array, and distributions of unique molecular identifiers per barcode (UMI), unique gene number per barcode, and percent of total UMIs corresponding to mitochondrial genes per barcode. **c**, Log normalized gene expression heatmap for top 10 marker genes by cell type (by log fold change vs. all others). **d**, Single-cell RNA-seq log normalized expression of known marker genes for stem, progenitor, Paneth, wound associated epithelium (WAE), and stress response, grouped by cell-type annotations. **e**, Heatmap of predicted pathway signaling for all human organoid cells using PROGENy scores calculated over single-cell RNA-seq data for each cell type. **f**, Human organoid UMAP labeled by annotated cell type, and split by treatment (control and KPT-330). **g**, Human organoid UMAP labeled by annotated cell type, and split by donor. **h**, Odds ratio enrichment and depletion by cell type and over donor based on Fisher exact testing with 95% confidence interval for each cell type relative to all others, dotted line at 1. FDR-adjusted Fisher exact testing; * $p < 0.05$, ** $p < 0.01$, *** $p < 0.001$, **** $p < 0.0001$, individual p-values reported in source data. **i**, Violin plots of module scores over all cells derived from genes with known nuclear export signals (NES) in all un-treated control cells split by non-stem, and stem G1S / G2M annotations, each score scaled on a range from 0 to 1 with below violin plot of XPO1 expression grouped by stem classification and split by treatment.



Extended Data Fig. 7 | Body weight and histological images of KPT-330-treated mice. **a**, Animal body weight over 14-day study, normalized per-animal to day 0, of vehicle or 10 mg/kg KPT-330, N = 4 biological replicates followed longitudinally. Two-way ANOVA, treatment variation $**p = 0.0017$. **b**, Animal body weight over 14-day study, normalized per-animal to day 0, of vehicle or 0.01, 0.05 or 0.2 mg/kg KPT-330. N = 12 biological replicates (0.01 and 0.05 mg/kg), N = 20 biological replicates (vehicle and 0.2 mg/kg) followed longitudinally. Two-way ANOVA, treatment variation $ns p > 0.05$. **c**, Representative images of small intestinal crypt histology (counted N > 30 crypts per animal, N > 12 animals per treatment) illustrating the range of 2 to 6 Paneth cells, stained with anti-lysozyme antibody. **d**, Histograms of Paneth cell number in proximal or distal small intestine of vehicle-treated animals. Cumulative frequency in proximal and distal small intestine of vehicle-treated animals was used for determining the cut-off value of Fig. 7C. N = 16 (vehicle and 0.2 mg/kg, proximal), N = 20 (vehicle and 0.2 mg/kg, distal), N = 12 (0.01 and 0.05 mg/kg, proximal and distal). **e**, Representative image of Olfm4⁺ stem cells in small intestinal crypts (counted N > 17 crypts per animal, N > 12 animals per treatment). **f**, Representative image of PAS⁺ goblet cells in small intestine (counted N > 15 crypts per animal, N > 12 animals per treatment).

Reporting Summary

Nature Research wishes to improve the reproducibility of the work that we publish. This form provides structure for consistency and transparency in reporting. For further information on Nature Research policies, see our [Editorial Policies](#) and the [Editorial Policy Checklist](#).

Statistics

For all statistical analyses, confirm that the following items are present in the figure legend, table legend, main text, or Methods section.

n/a Confirmed

- | | | |
|-------------------------------------|-------------------------------------|--|
| <input type="checkbox"/> | <input checked="" type="checkbox"/> | The exact sample size (n) for each experimental group/condition, given as a discrete number and unit of measurement |
| <input type="checkbox"/> | <input checked="" type="checkbox"/> | A statement on whether measurements were taken from distinct samples or whether the same sample was measured repeatedly |
| <input type="checkbox"/> | <input checked="" type="checkbox"/> | The statistical test(s) used AND whether they are one- or two-sided
<i>Only common tests should be described solely by name; describe more complex techniques in the Methods section.</i> |
| <input type="checkbox"/> | <input checked="" type="checkbox"/> | A description of all covariates tested |
| <input type="checkbox"/> | <input checked="" type="checkbox"/> | A description of any assumptions or corrections, such as tests of normality and adjustment for multiple comparisons |
| <input type="checkbox"/> | <input checked="" type="checkbox"/> | A full description of the statistical parameters including central tendency (e.g. means) or other basic estimates (e.g. regression coefficient) AND variation (e.g. standard deviation) or associated estimates of uncertainty (e.g. confidence intervals) |
| <input type="checkbox"/> | <input checked="" type="checkbox"/> | For null hypothesis testing, the test statistic (e.g. F , t , r) with confidence intervals, effect sizes, degrees of freedom and P value noted
<i>Give P values as exact values whenever suitable.</i> |
| <input checked="" type="checkbox"/> | <input type="checkbox"/> | For Bayesian analysis, information on the choice of priors and Markov chain Monte Carlo settings |
| <input checked="" type="checkbox"/> | <input type="checkbox"/> | For hierarchical and complex designs, identification of the appropriate level for tests and full reporting of outcomes |
| <input type="checkbox"/> | <input checked="" type="checkbox"/> | Estimates of effect sizes (e.g. Cohen's d , Pearson's r), indicating how they were calculated |

Our web collection on [statistics for biologists](#) contains articles on many of the points above.

Software and code

Policy information about [availability of computer code](#)

Data collection Single-cell RNA sequencing data were generated using the Illumina NovaSeq 6000 and NextSeq 550. Flow-cytometry data were collected on a BD LSR Fortessa. Fluorescence assay data were collected on a Tecan M1000 Plate Reader.

Data analysis Sequencing data was de-multiplexed using bcl2fastq v2.20.0.422, and seq-well FASTQs were aligned and processed using the Drop-Seq computational protocol v2.3.0 (<https://github.com/broadinstitute/Drop-seq>). For antibody hashing experiment, CITE-seq-Count v1.4.2 was used. R v4.0 and associated packages (tidyverse v1.3.0, Seurat v3.1.5, DescTools v0.99.36, scales v1.1.1, ggplot2 v3.3.1, superheat v0.1.0, Matrix v1.2-18, piano v2.4.0, RColorBrewer v1.1-2, viridis v0.5.1, effectsize v0.3.1, crunch v1.26.3, progeny v1.10.0, dorothea v1.0.0, viper v1.22.0) were used to analyse sequencing data. Further analyses were performed using R, Prism for macOS Version 8.3, and FlowJo X Version 10.6.1. Image quantification was performed with Fiji v2.0. Analysis scripts for screening and for single-cell RNA-seq are available at https://github.com/ShalekLab/Mead_et_al_NatBME_2021.

For manuscripts utilizing custom algorithms or software that are central to the research but not yet described in published literature, software must be made available to editors and reviewers. We strongly encourage code deposition in a community repository (e.g. GitHub). See the Nature Research [guidelines for submitting code & software](#) for further information.

Data

Policy information about [availability of data](#)

All manuscripts must include a [data availability statement](#). This statement should provide the following information, where applicable:

- Accession codes, unique identifiers, or web links for publicly available datasets
- A list of figures that have associated raw data
- A description of any restrictions on data availability

Source data for the figures are provided with this paper. The accession number for the murine single-cell RNA-sequencing data is available from the NCBI Gene

Expression Omnibus under accession number GSE148524. Interactive visualization tools, metadata and digital gene-expression matrices can be found via the Broad Institute's Single-Cell Portal (<https://singlecell.broadinstitute.org>; studies SCP1547 and SCP1318). To protect the genetic information of donors, FASTQ data for the human intestinal organoids is available on request from A.S., provided that a data-use agreement can be signed. The ValidNESS database was accessed via <http://validness.ym.edu.tw>.

Field-specific reporting

Please select the one below that is the best fit for your research. If you are not sure, read the appropriate sections before making your selection.

Life sciences Behavioural & social sciences Ecological, evolutionary & environmental sciences

For a reference copy of the document with all sections, see [nature.com/documents/nr-reporting-summary-flat.pdf](https://www.nature.com/documents/nr-reporting-summary-flat.pdf)

Life sciences study design

All studies must disclose on these points even when the disclosure is negative.

Sample size	For the animal-model analyses, we performed a power analysis to estimate the appropriate number of animals. No statistical tests were used to determine sample sizes for other experiments; sample size was determined from prior experience and from pilot experiments, and at least three biological replicates were used for each experiment (except for single-cell RNA sequencing).
Data exclusions	For PAS+ goblet-cell counting, histological samples that included < 15 countable villi were excluded. PAS+ cell-number variation was large, and it was difficult to collect many countable villi per sample; hence, the point of compromise was 15 (this exceeded the recommended count number, in consultation with a pathologist). Otherwise, no data were excluded from the analyses.
Replication	All experiments were performed in at least three independent biological replicates, except for single-cell RNA sequencing, where a single sample contained single cells derived from thousands of organoids of identical condition. Where applicable, all attempts at replication were successful.
Randomization	For the animal study, mice were randomly allocated to each group. For the cell-based analyses and screening, wells were randomly assigned for each treatment.
Blinding	For histological analyses, the slides were blinded before counting. Otherwise, the samples were not blinded; they were randomized for practical expediency.

Reporting for specific materials, systems and methods

We require information from authors about some types of materials, experimental systems and methods used in many studies. Here, indicate whether each material, system or method listed is relevant to your study. If you are not sure if a list item applies to your research, read the appropriate section before selecting a response.

Materials & experimental systems

n/a	Involved in the study
<input type="checkbox"/>	<input checked="" type="checkbox"/> Antibodies
<input checked="" type="checkbox"/>	<input type="checkbox"/> Eukaryotic cell lines
<input checked="" type="checkbox"/>	<input type="checkbox"/> Palaeontology and archaeology
<input type="checkbox"/>	<input checked="" type="checkbox"/> Animals and other organisms
<input type="checkbox"/>	<input checked="" type="checkbox"/> Human research participants
<input checked="" type="checkbox"/>	<input type="checkbox"/> Clinical data
<input checked="" type="checkbox"/>	<input type="checkbox"/> Dual use research of concern

Methods

n/a	Involved in the study
<input checked="" type="checkbox"/>	<input type="checkbox"/> ChIP-seq
<input type="checkbox"/>	<input checked="" type="checkbox"/> Flow cytometry
<input checked="" type="checkbox"/>	<input type="checkbox"/> MRI-based neuroimaging

Antibodies

Antibodies used

FITC-conjugated anti-lysozyme antibody (Dako, F0372), APC-conjugated anti-CD24 antibody (Biolegend, #138505), anti-lysozyme antibody (Abcam, ab108508), HRP-linked anti-rabbit IgG antibody (Cell Signaling, #7074), anti-Ki67 antibody (BD Biosciences, #550609), anti-Olfm4 antibody (Cell Signaling, #39141), anti-Lysozyme (Thermo Fisher Scientific, RB-372-A), anti-E-cadherin (Thermo Fisher Scientific, 13-1900), anti-Rat IgG (H+L) Highly Cross-Adsorbed Secondary Antibody, Alexa Fluor 488 (Thermo Fisher Scientific, A21208), anti-Rabbit IgG (H+L) Highly Cross-Adsorbed Secondary Antibody, Alexa Fluor 568 (Thermo Fisher Scientific, A10042).

Validation

FITC-conjugated anti-lysozyme antibody (Dako, F0372) and anti-CD24 antibody (Biolegend, #138505) were validated in some previous studies such as BMC Biology 16, 62 (2018).

anti-Lysozyme (Thermo Fisher Scientific, RB-372-A) was validated in some previous studies such as Cell, 178, 5, 1115, 2019 and by the manufacturer (<https://www.fishersci.se/shop/products/lab-vision-lysozyme-muramidase-ab-1-rabbit-polyclonal-antibody-bsa-azide/12603267?searchHijack=true&searchTerm=12603267&searchType=RAPID&matchedCatNo=12603267>).

anti-E-cadherin (Thermo Fisher Scientific, #13-1900) was validated in some previous studies such as J Cell Biol., 204, 839, 2014 and by the manufacturer (<https://www.thermofisher.com/antibody/product/E-cadherin-Antibody-clone-ECCD-2-Monoclonal/13-1900>).

anti-Rat IgG (H+L) Highly Cross-Adsorbed Secondary Antibody, Alexa Fluor 488 (Thermo Fisher Scientific, A21208) and anti-Rabbit IgG (H+L) Highly Cross-Adsorbed Secondary Antibody, Alexa Fluor 568 (Thermo Fisher Scientific, A10042) were validated in many previous studies and by the manufacturer (<https://www.thermofisher.com/antibody/product/Donkey-anti-Rat-IgG-H-L-Highly-Cross-Adsorbed-Secondary-Antibody-Polyclonal/A-21208> and <https://www.thermofisher.com/antibody/product/Donkey-anti-Rabbit-IgG-H-L-Highly-Cross-Adsorbed-Secondary-Antibody-Polyclonal/A10042>).

anti-lysozyme antibody (Abcam, ab108508) was validated in some previous studies such as Nature Communications 11, 37 (2020) and by the manufacturer (<https://www.abcam.co.jp/lysozyme-antibody-epr29942-ab108508.html>).

anti-Ki67 antibody (BD Biosciences, #550609) was validated in some previous studies such as Nature Communications 9, 485 (2018) and by the manufacturer (<https://wwwbdbiosciences.com/us/applications/research/intracellular-flow/intracellular-antibodies-and-isotype-controls/anti-rat-antibodies/purified-mouse-anti-ki-67-b56/p/550609>).

anti-Olfm4 antibody (Cell Signaling, #39141) was validated in some previous studies such as Cell Reports 24, 2312-2328.e7 (2018) and by the manufacturer (https://www.cellsignal.jp/products/primary-antibodies/olfm4-d6y5a-xp-rabbit-mab-mouse-specific/39141?_=1597801405085&Ntt=39141&tahead=true).

Animals and other organisms

Policy information about [studies involving animals](#); [ARRIVE guidelines](#) recommended for reporting animal research

Laboratory animals	8–10-week-old wild type C57BL/6NcrJ male mice (#027) were purchased from Charles River. The mice were housed under 12-h light/dark cycles, and provided food and water ad libitum. They were kept at 20–22 °C and in a 30–70% humidity environment.
Wild animals	The study did not involve wild animals.
Field-collected samples	The study did not involve samples collected from the field.
Ethics oversight	All animal studies were approved by the Committee on Animal Care (CAC) at Massachusetts Institute of Technology.

Note that full information on the approval of the study protocol must also be provided in the manuscript.

Human research participants

Policy information about [studies involving human research participants](#)

Population characteristics	De-identified adult duodenal tissue was collected during bulk surgical resection and distributed as excess surgical tissue via MGH pathology. Donors were of both sexes, aged 58–74 years old, with pathologies presumed to have no impact on the duodenum.
Recruitment	Small intestinal crypts were isolated from de-identified human bulk surgical resections.
Ethics oversight	All studies were performed under protocols approved by the Massachusetts Institute of Technology (MIT) Committee on the Use of Humans as Experimental Subjects, and excess surgical tissue was collected under Mass General Brigham Protocol 2010P000632, in accordance with IRB guidance.

Note that full information on the approval of the study protocol must also be provided in the manuscript.

Flow Cytometry

Plots

Confirm that:

- The axis labels state the marker and fluorochrome used (e.g. CD4-FITC).
- The axis scales are clearly visible. Include numbers along axes only for bottom left plot of group (a 'group' is an analysis of identical markers).
- All plots are contour plots with outliers or pseudocolor plots.
- A numerical value for number of cells or percentage (with statistics) is provided.

Methodology

Sample preparation	Organoids were harvested from Matrigel by mechanical disruption in TrypLE Express (Thermo, #12605010) to remove the Matrigel and to dissociate the organoids into single cells. See Methods for details.
Instrument	We used LSR Fortessa (BD; Koch Institute Flow Cytometry Core at MIT).
Software	The data were analysed using FlowJo X v10.6.1 software.

Cell population abundance

Approximately 50% of the objects detected by the flow were identified as single cells, and about 25–60% of the single cells were alive. All live cells were analysed to calculate the Paneth-cell population.

Gating strategy

FSC and SSC were used for selecting single cells, and live cells were identified as Zombie Violet-negative cells. Extended Data Fig. 1f provides details.

Tick this box to confirm that a figure exemplifying the gating strategy is provided in the Supplementary Information.